Title
Fast biomedical imaging using fluorescence lifetime and unique Raman signatures

Author
Papour, Asael

Publication Date
2015

Peer reviewed|Thesis/dissertation

UNIVERSITY OF CALIFORNIA

Los Angeles

Fast biomedical imaging using fluorescence lifetime and unique Raman signatures

A dissertation submitted in partial satisfaction of the

requirements for the degree Doctor of Philosophy

in Electrical Engineering

by

Asael Papour

2015

ABSTRACT OF THE DISSERTATION

Fast biomedical imaging using fluorescence lifetime and unique Raman signatures

By

Asael Papour

Doctor of Philosophy in Electrical Engineering

University of California, Los Angeles, 2015

Professor Oscar M. Stafsudd, Chair

Abstract:

Failed wounds in the extremities are characterized with abnormal collagen production and inappropriate bone growth in soft tissue. This condition can occur after trauma to a limb and can cause a disruption to the healing process, and is known as Heterotopic Ossification (HO). In HO, regions in the tissue start to mineralize and form microscopic bone-like structures. These structures continue to calcify and develop into large, non-functional bony masses that cause pain, limit limb movement, and expose the tissue to reoccurring infections; in the case of open wounds this can

lead to amputation as a result of a failed wound. Both Magnetic Resonance Imaging (MRI) and X-ray imaging have poor sensitivity and specificity for the detection of HO, thus delaying therapy and leading to poor patient outcomes. This work presents a bi-modality approach using real-time fluorescence lifetime imaging and Raman imaging for tissue differentiation. The fluorescence system is based on relative lifetime contrast generation to characterize surface tissue morphology and detect margins of abnormal tissue, specifically connective tissue biomarkers. The Raman system utilizes a biocompatible, fast, and a large field of view (1 cm^2) acquisition to differentiate bone tissue from soft tissue without using a spectrometer, this is in contrast to conventional Raman microscopy systems. This capability may allow for the development of instrumentation which permits bedside complementary diagnosis of HO.

The dissertation of Asael Papour is approved.

Warren D. Grundfest

Daniel Ennis

Oscar M. Stafsudd, Committee Chair

University of California, Los Angeles

2015

Table of Contents

Introduction 1

Fluorescence Lifetime Imaging Microscopy (FLIM) background 3

Real-time fluorescence lifetime imaging – a contrast based approach 7

Image acquisition and processing 8

System design 13

Gate Characteristics 14

Illumination and contrast generation using LEDs 15

Sensitivity and limitations 16

Optical imaging for brain tissue characterization using relative fluorescence lifetime imaging .. 18

Ex vivo Retinal Imaging of Porcine Eyes with Preservation of Intraocular Pressure and Shape . 28

Imaging auto-fluorescence temporal signatures of the human ocular fundus in vivo 37

Raman Stokes scattering background 50

Raman imaging systems comparison 52

Wide-field Raman imaging for bone detection in tissue 55

Future efforts 70

List of Figures:

Figure 1. Acute wound healing process 1

Figure 2. Exponential decay measurement and fitting (red) upon short pulse excitation (blue) 6

Figure 3. Illumination and recording algorithm 9

Figure 4. Image normalization 11

Figure 5. Fluorescence imaging system setup. 19

Figure 6. Relative fluorescence lifetime algorithm. 21

Figure 7. The bread slice loafing employed by the BTTR. 23

Figure 8. Brain tissue imaging results. 24

Figure 9. Corneal edema in a porcine eye. 29

Figure 10. Cage system for ex vivo fundus imaging 30

Figure 11. Porcine eye in the windowed cage system 32

Figure 12. Cage assembly with added external lens and a color fundus image. 34

Figure 13. Relative fluorescence lifetime algorithm. 38

Figure 14. Modified fundus camera 41

Figure 15. ex vivo porcine eye imaging using fundus camera. 42

Figure 16. Fundus images of 3 patients. 43

Figure 17. Molecular scattering energies correspond to mass and bond's strength 50

Figure 18. Raman Stokes scattering..... 51

Figure 19. Raman systems performance comparison 52

Figure 20. Imaging system schematics. 60

Figure 21. Fluorescence and Raman spectrum and imaging algorithm..... 61

Figure 22. Bone on tissue imaging 63

Figure 23. Bone on tissue imaging with microCT projections 64

Figure 24. Bone embedded in tissue imaging with microCT projections..... 64

Figure 25. Raman and Fluorescence spectra utilization 71

Acknowledgements

This work was supported by the Telemedicine & Advanced Technology Research Center (TATRC) of the US Army Medical Research and Materiel Command (USAMRMC), as part of the DoD medical research program under Award # W81XWH-12-2-0075.

Publications and conferences:

"Multi-Spectral Fluorescence Lifetime Contrast Imaging for Brain Cancer Detection," Biomedical Engineering Society (BMES) conference presentation, Atlanta 2012.

A. Papour, Z. Taylor, A. Sherman, D. Sanchez, G. Lucey, L. Liau, O. Stafsudd, W. Yong, and W. Grundfest, "Optical imaging for brain tissue characterization using relative fluorescence lifetime imaging," J. Biomed. Opt. 18, 060504–060504 (2013).

A. J. Sherman, A. Papour, S. Bhargava, "Normalized fluorescence lifetime imaging for tumor identification and margin delineation," Proc SPIE 8572, vol. Advanced Biomedical and Clinical Diagnostic Systems XI, Mar. 2013.

“Wide-Field Convolved Spectro-temporal Fluorescence Signatures Acquisition System - A Nontraditional Video-Rate Imaging Technique,” Annual Research Review (ARR) presentation, UCLA 2013.

A. Papour, Z. Taylor, O. Stafsudd, I. Tsui, and W. Grundfest, “Imaging auto-fluorescence temporal signatures of the human ocular fundus in vivo,” J. Biomed. Opt. (Accepted, 2015).

A. Papour, J. H. Kwak, Z. Taylor, B. Wu, O. Stafsudd, W. Grundfest, “Wide-field Raman imaging for bone detection in tissue,” Biomed. Opt. Express, (Accepted, 2015).

A. Papour, Z. Taylor, O. Stafsudd, W. Grundfest, “Real time early detection system of failed wounds and heterotopic ossification imaging system using unique Raman signatures,” Proc. SPIE 9417, Medical Imaging 2015; doi:10.1117/12.2082093.

“Rapid optical imaging for brain tissue characterization and biobanking using contrast based spectro-temporal autofluorescence signatures," Society for Brain Mapping and Therapeutics conference, LA 2015.

"Real time early detection imaging system of failed wounds and heterotopic ossification using unique Raman signatures," SPIE Medical Imaging, Orlando 2015.

VITA

2008	B.Sc. in Physics & Chemistry Hebrew University of Jerusalem Jerusalem, Israel
2009-2010	Contractor Pacific Gas & Electric (PG&E) Los Altos Hills, California
2010-2013	Teaching Assistant and Graduate Student Researcher University of California, Los Angeles Los Angeles, California
2012	M.Sc. in Electrical Engineering University of California, Los Angeles Los Angeles, California Thesis: Analysis and Optimization of a Lifetime Fluorescence System to Detect Structural Protein Signatures in Varying Host Mediums for Rapid Biomedical Imaging.

2012-2015 Ph.D. Candidate in Electrical Engineering

University of California, Los Angeles

Los Angeles, California

Introduction

The problem we were set to investigate was motivated by the Department of Defense (DoD) and the US Army's need for an early detection system for failed wounds in the extremities, as part of the failed wound initiative. Combat wounds in the limbs, are characterized as an acute injury in which profound mass of tissue is destroyed. Acute wound healing is an ordered process of time-dependent events (Figure 1) that starts at the time of injury and results in tissue repair.

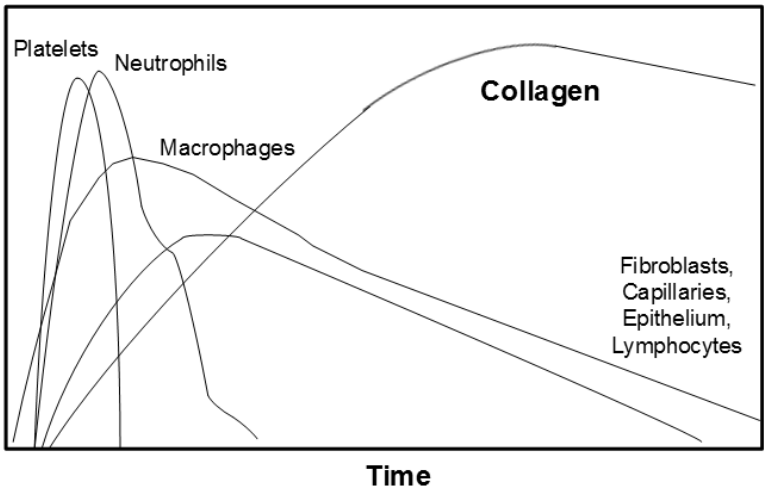

Figure 1. Acute wound healing process

D. A. Dubay and M. G. Franz, "Acute wound healing: the biology of acute wound failure," Surg. Clin. North Am. 83(3), 463–481 (2003) [doi:10.1016/S0039-6109(02)00196-2].

In failed wounds, for reasons that are not completely understood, the healing process is interrupted; abnormalities in collagen formation are observed, and bone-like structures start to appear and grow in the tissue. The bone growth is called Heterotopic Ossification (HO) and not all abnormalities in collagen are indicative of HO formation. HO is difficult to detect with conventional imaging methods such as X-ray and Magnetic Resonance Imaging (MRI), due to their low sensitivity and specificity. This difficulty results in failure to diagnose HO in its early stages and can lead to intervention by surgery, potentially exposing the patient to reoccurring infections, and can eventually lead to amputation in order to not risk the patient's life. Medication can be prescribed but due to delayed detection and severe side effects, the effectiveness is low.

The goal of this research is to utilize fluorescence lifetime imaging for fast surface tissue differentiation, specifically imaging fibrous tissue and margin detection of abnormal tissue, and a complementary Raman imaging for surface and in-depth, high specificity bony structures detection.

This work is comprised of two main sections; the fluorescence imaging and the Raman imaging systems. Both are designed to achieve safe bio-compatible operation, with a large field of view (1 cm^2) and fast imaging rate (~1 frame per second). These advantages hold the potential to remove the hurdles and accept Fluorescence Lifetime Imaging Microscopy (FLIM) and Raman imaging modality in the clinical setting and to serve as point of care diagnostic tools to ultimately improve patient outcomes.

Fluorescence Lifetime Imaging Microscopy (FLIM) background

Ultra Violet (UV) radiation is part of the electromagnetic spectrum, between the visible and X-ray regions and spans from Extreme-UV at 10 nm (nano-meters, 10-9 meters) to visible violet at 400 nm. Most of the UV spectra, Extreme to Middle UV (10 – 300 nm) is absorbed by the atmosphere and does not propagate to long distances. UV radiation is used in many applications in black-light activated technologies and serves different purposes at various wavelength bands; Near-UV 300 – 400 nm is used in security measures and counterfeit detection, Middle-UV 200 – 300 nm used in disinfection devices since it has more potential in damaging tissue and can cause severe damage to DNA (Sinha and Hader 2002), and Far-UV 100 – 200 nm that is used in the semiconductor industry for photolithography and in medicine for eye surgeries (LASIK), ablating material without heating the tissue.

The technologies that are based on the less energetic Near-UV light (300-400 nm), propagate well in the atmosphere and are used to explore the light-material interaction to detect chemicals that otherwise are left invisible. The emitted light is the fluorescence response of the added chemicals (fluorophores) that are visible to the naked eye under UV illumination. Some fluorophores emit broadband light which appears to be toned white, while others are engineered to fluoresce in a narrow regime of the spectrum and show a pronounced color.

Proteins in our body including metabolic, structural and others, each revealing a unique auto-fluorescence spectrum that can be identified and mapped within the tissue or individual cells.

Looking at intensities and color distribution (spectrum) of the emitted light using amplitude fluorescence technique, much can be learned on cellular organization and mechanisms, tissue morphology and structure (Ramanujam 2000). This technology has shown good results in imaging materials, however, it encountered many difficulties in tissue. Differentiation between endogenous fluorophores is less accurate in cluttered environment and is sensitive to scattering and absorption and misrepresents the true content of the tissue.

In order to overcome these shortcomings, another aspect of fluorescence emission has been investigated and shown to have improved detection capabilities especially in high variability and clutter-dominated tissue. By looking at the fluorescence intensity in time, after a short excitation pulse of UV light, the time dependent behavior of the emitted signal can be recorded and analyzed. This technique can characterize tissue with higher sensitivity and specificity (80%-90%) (Tadrous et al. 2003). Fluorescence emission is a process in which the molecule releases the energy of the absorbed UV light, to relax back into a stable state with lower energy. This is done by emitting light at a longer wavelength (often visible).

Fluorescence Lifetime Imaging Microscopy (FLIM) is a research technique that extracts the auto-fluorescence lifetime from the fluorescence intensity decay at each point on the tissue sample, and delineates tissue constituents based on variations in decay time. This is accomplished by exciting the sample with a very short (pico second) pulse of a UV laser, and detecting the auto-fluorescence decay coefficient at a range of wavelengths (Lakowicz 2006; Sun et al. 2010; Marcu et al. 2004).

The fluorescence decay rate is governed by the specific molecular energy levels structure: Slow relaxation mechanisms will reveal longer fluorescence decay emission, while fast energy

relaxation, which is an increase in probability for relaxation, will reveal a short fluorescence decay behavior. This added observation, of energy levels configuration and relaxation rate, is a detailed indicator of molecular and chemical structure that results in greater detection specificity (Lakowicz 2006). Energy levels and relaxation processes can also be sensitive to environmental changes: Acidity (pH), pressure, temperature, and proximity of other molecules or proteins, and cause temporal and spectral changes to the emitted fluorescence signals. These changes can serve as indicators for tissue health and monitor metabolic processes (Lakowicz 2006).

Traditional time-resolved fluorescence imaging techniques, such as FLIM, measures the intensity decay profile point by point consecutively in time. This method records the fluorescence decay profile in steps to recreate a theoretical model that can fit and estimate the decay shape characteristics. Fluorescence decay is a statistical phenomenon that can be closely estimated and described mathematically by an exponential decay function. The radiative rate of decay is governed by the parameter τ (Greek, Tau) that represents the fluorescence lifetime of a material with a simple single exponential behavior (eq.1).

$$F(t) = e^{\frac{-t}{\tau}}$$

Eq. 1 is a normalized function.

A theoretical line can be drawn to fit the data points in a shape of an exponential decay function to estimate and extract the characteristic lifetime coefficient (Figure 2).

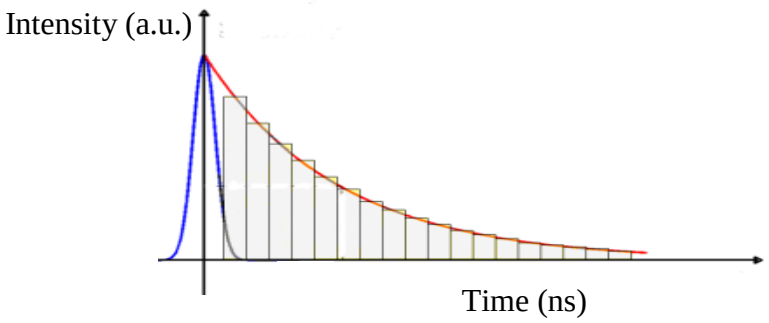

Figure 2. Exponential decay measurement and fitting (red) upon short pulse excitation (blue)

Decay rates are dependent on the biochemical composition of the material, and significant contrast can be generated using maps of decay times. Time resolved fluorescence is superior to amplitude fluorescence, since the fluorophores' lifetime is not related to fluorescence intensity and does not depend on factors that would significantly degrade amplitude only measurements such as; concentration, absorption, and scattering by tissue surface geometry. However, this technique has not transcended the research and development stage into the clinical level due to several limiting factors. Data processing of the large recorded datasets is computationally intensive and uses methods of lifetime extraction, for example via orthogonal basis calculation (Laguerre polynomials), to identify fluorophore decay times and distributions (Phipps et al. 2012; Maarek et al. 2000; Jo, Fang, and Marcu 2005; De Veld et al. 2005; Wagnieres, Star, and Wilson 1998). This powerful approach is slow and prone to significant errors as Signal to Noise Ratio (SNR) drops (Jo, Fang, and Marcu 2005). Moreover, the solution is not unique and requires setting a-priori

assumptions that can oversimplify the complex nature of the decay behavior (Lakowicz 2006). There exists no robust, objective manner to choose the number of terms in the formula, and different numbers of terms can all produce good fits but provide completely different interpretations of the results. Another limiting factor is found in the image acquisition routine; low signal levels require a longer measurement time in order to produce better fitting results, hence a typical acquisition time for a large field of view (> 0.5 mm) including processing time is in the order of a few minutes per lifetime image (Jo, Fang, and Marcu 2005). To overcome these limitation, many systems are based on single point spectroscopy and photon-counting techniques or small field of view optical fiber bundle. Point spectroscopy, for example, requires mechanical scanning to create a 2D image and has hindered the clinical acceptance of this technique.

Real-time fluorescence lifetime imaging – a contrast based approach

A new paradigm utilizes the differences in lifetime signatures and converts them directly to a contrast image, without any lifetime calculations (Papour et al. 2013; Jiang, Grundfest, and Stafsudd 2011). By changing the illumination profile and the processing methods, the new scheme enables a fast measurement that encapsulates the lifetime property without calculation of the decay coefficient. This system combines a long illumination period (compared with pico second lasers) and a normalization algorithm to produce direct contrast. The resulting fluorescence contrast images are based on lifetime differences. By avoiding calculation of lifetimes, a tremendous gain in total acquisition and processing time is achieved compared to traditional FLIM that uses the shortest illumination pulse possible to brute-force a fluorescence lifetime decay coefficient measurement. Variance in constituent concentration and location are seen as changes in contrast,

similar to the way X-rays create a contrast based on relative changes in density. Constituents such as fat, collagen, elastin, NADH etc. dominate the lifetime map, with the level of expression dependent on the detection wavelength, due to their unique fluorescence signature. These maps can show normal and abnormal distributions of constituents, and lead to a better understanding of the tissue complexity and biochemical structure. As a result, the contrast maps are a sensitive indication for tumor boundaries and other abnormalities, including the integrity of the tissue sample. Understanding and visualizing chemical and morphological changes on the tissue's surface has the potential to delineate tissue abnormalities during surgical procedures.

Image acquisition and processing

The image processing procedure encapsulates a key capability of the system: By dividing two acquired fluorescence images pixel to pixel division, normalization is performed and the resulting value is a representative of the fluorescence decay rate. Higher values represent longer fluorescence lifetimes, while lower values represent shorter lifetimes. The imaging methodology encompasses acquisition of only two images; the first image is taken during excitation and is referred to as the 'calibration image', while the second image is taken during the fluorescence decay and referred to as the 'decay image' (Figure 3).

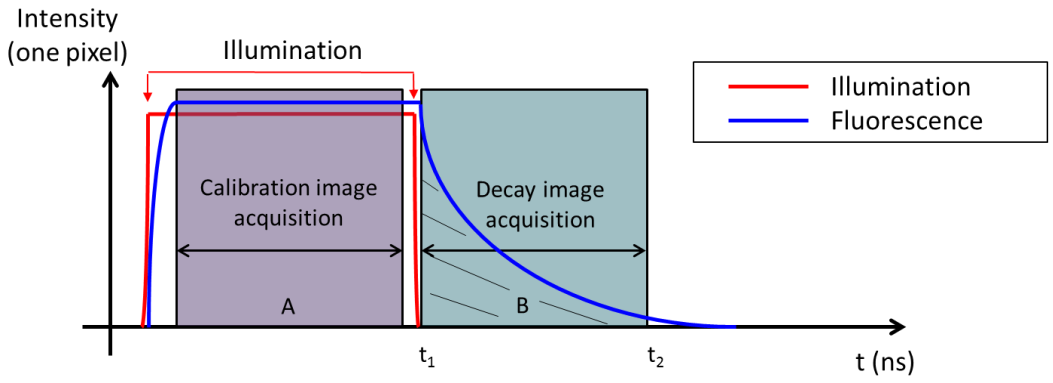

Figure 3. Illumination and recording algorithm

$$A = \eta P \Delta t = I_0 \Delta t$$

Eq. 2 Area A in Figure 2 represents fluorescence yield at steady state. P- Pump power, η- yield

$$B = \eta P \int_{t_1}^{t_2} e^{-\frac{t}{\tau}}\, dt = I_0 \tau \left(e^{-\frac{t_1}{\tau}} - e^{-\frac{t_2}{\tau}}\right) \approx \boldsymbol{I_0 \tau}$$

Eq. 3 Area B in Figure 2 represents integration of the fluorescence decay

$$t_1 \ll \tau \ , \ t_2 \gg \tau$$

Eq. 4 The approximation of B is valid under acquisition parameters t_1 and t_2

The calibration image is acquired during the LEDs' constant illumination for ~10 ns and then saved. This image holds important information of the fluorescence yield and locality. By looking

at the steady state intensity, we can eliminate scattering and absorption factors and ultimately be sensitive to the lifetime factor alone. Next, the LEDs are turned off and the second image is acquired during the fluorescence decay for a period of ~10 ns, depending on the tissue type. The decay image is recording the unique decay signatures of the tissue at each location (pixel). In this acquisition system, all of the pixels are acquired in parallel using conventional imaging optics.

In the processing stage, the decay image is divided by the calibration image to create a relative lifetime decay map: Each pixel's intensity value in the decay image is divided with the corresponding pixel in the calibration image. This results in a final relative lifetime image (normalized image) (Figure 4). This method creates contrast by taking only two images; one during illumination and the second during the decay period. By dividing the decay signature with its corresponding steady state fluorescence yield, a quotient that correlates only to lifetime is accomplished.

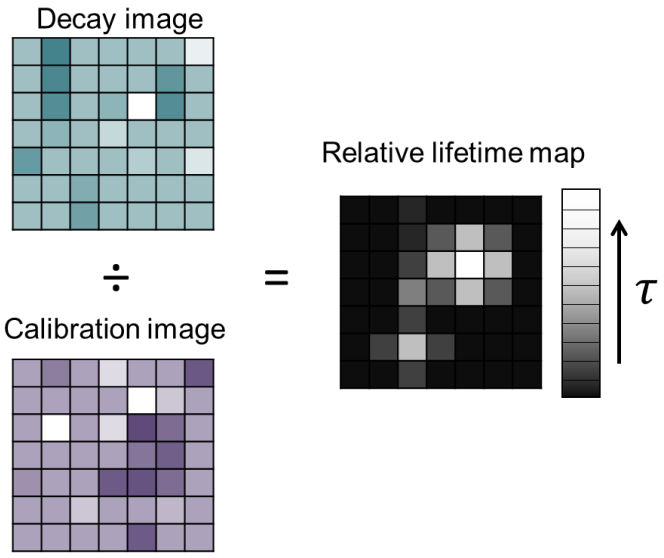

Figure 4. Image normalization

$$\frac{B}{A} = \frac{I_0 \quad \tau}{I_0 \quad \Delta t} \propto \boldsymbol{\tau}$$

Eq. 5 Normalization produces a final image that relies only on lifetime coefficients

Variation in lifetime on the tissue surface will reveal image contrast of the different corresponding locations. A larger quotient means a long relative lifetime while a smaller quotient represents a shorter lifetime. This procedure results in pronounced contrast images with high SNR due to the acquisition metrics; each pixel is integrating the intensity of the fluorescence signal during the acquisition periods, and allows for the total imaging time to be very short, less than one second.

This measurement can be repeated in many different excitation and collection wavelengths using various LEDs and band-pass filters to divide the spectrum and isolate individual constituents for

better contrast and increased specificity. The ability to create multi-spectral imaging can also increase sensitivity to find higher order correlations of normal vs. abnormal tissue locations.

Finding lifetime information in a relative type measurement method is similar to X-ray, and Magnetic Resonance Imaging (MRI), where contrast is the result of local changes in density or concentration, respectively. This new modality displays optical variation in tissue by morphological and density changes of the constituents in the top layers of the tissue, to reveal features that are not visible to the naked eye. The analogy to X-ray and MRI serves as a good comparison to modalities in which maps of relative measurements are used. These modalities do not supply absolute measurements and yet serve as a powerful tool for diagnostics. The fast autofluorescence contrast imaging modality is compatible with clinical settings, since the short acquisition time eliminates blur and signal degradation due to natural movements; pulse, breathing etc. In comparison to conventional FLIM systems, the relative measurement system yields a hundred fold decrease in acquisition time and ten thousand fold decrease in processing time. This novel system also eliminates common problems of FLIM such as damage to the tissue and photo-bleaching due to the high peak power of lasers by using LED technology with long flat-top pulses and low peak power. Since processing for image generation requires only simple mathematical operations, it is possible to process an entire image with good contrast at video rate with the minimal processing power found on every mobile computer platform. Since this method does not require fluorophore lifetimes extraction, the illumination pulse widths can vary from 1 to 20 ns depending on tissue type. This avoids the need for an expensive, bulky, pulsed UV laser and permits the use of inexpensive, compact LEDs (Asael Papour 2013; Kennedy et al. 2008; Jiang,

Grundfest, and Stafsudd 2011; Sherman et al. 2013; Papour et al. 2013). Acquisition can be completed in less than 1 second while processing time is ~5 milliseconds for a 100 mm^2 field of view at ~35 μm resolution.

System design

A key component of the system is the imager; a camera that is capable of recording nano-second events at high rates. Intensified camera or, Intensified Coupled Charged Device (iCCD) is a camera type that has an intensifier unit in front of the CCD. This module operates as the shutter and as an amplifier, capable of increasing the sensitivity of the device in low light conditions. A photocathode film captures the incident image light at visible wavelengths (400 - 700 nm) in front of the camera, and generates photoelectrons by means of the photoelectric effect. The emitted electrons are drawn inside the camera into an intensifier tube by an applied electric field. The intensifier tube is comprised of a micro channel plate (MCP), which operates under high voltage to accelerate electrons, and multiply them in a chain reaction that amplifies the signal to a thousand fold. After passing through the MCP, the electrons collide on a green phosphorous layer to generate photons to be collected on the CCD. In nanosecond exposure conditions, high voltage across the MCP is switched by an electronic circuit to operate as the shutter and amplifies the incoming image. Although a small signal can be collected on the CCD in one short exposure (of few nanoseconds), in conditions of a repetitive signal, data can be timely sampled and accumulated on the CCD to generate an image that otherwise would not be detected.

Gate Characteristics

The intensifier's efficiency in passing an optical signal is a complex function of the device assembly and the operational settings. The gating mechanism is capable of transmitting the optical signals in a gate period as short as 100 ps. This short gating time is achieved at the expanse of low signal intensity due to inefficiencies of the image intensifier. The efficiency is defined by the percentage intensity of an incoming signal that passes through the intensifier. Longer gate times result in significantly better transmission efficiency and serve as another factor for using long gate times. Traditional FLIM requires short (sub-nanosecond) gate times in order to achieve a good resolution decay curve. With low gating efficiency however, it will take longer to achieve an adequate image. In comparison to the contrast measurement system, operation of considerably longer gate times of 10 ns is used. A high image transmission efficiency of almost a hundred percent is reached. This further reduces the total image acquisition time and optimizes the performance of the system. These benefits serve as an additional advantage when using long shutter times in this system to achieve real-time imaging.

The resolution of the camera is set by a few parameters, and unlike a regular CCD, iCCD cameras are usually inferior in resolution. The MCP channel's size of 25 μm in diameter, and further restrictions of the phosphorous layer and other properties, all contribute to degradation of the observed image in the camera's final output.

Illumination and contrast generation using LEDs

Another key advantage of the system architecture, is the circular array of light emitting diodes about the lens aperture. LEDs can easily illuminate a large tissue area with good uniformity without the need for complicated optics. They often include a built-in lens that makes the set-up very compact, unlike lasers which require fiber optics to guide the light to the tissue and a tailored optics solution to uniformly illuminate the tissue surface. Beyond LEDs evident cost effectiveness and robustness, a major consideration in choosing them over lasers is that they do not require the same regulatory compliance that lasers must acquire for use in medical devices.

Sensitivity and limitations

The system has proven the ability to distinguish between fluorophores with less than 6% difference in lifetime (Jiang, Grundfest, and Stafsudd 2011). In imaging tissue, clutter and noise dominate the lifetime map and limit the detection rate for small abnormalities. Factoring in noise and a decrease in resolution, sensitivity will decrease but will depend on the type of tissue. Continuing study of the system's performance and large statistical analysis is undergoing and will reveal the detection rate and sensitivity of the system in different tissue types.

Limitations:

The system is designed to achieve good contrast in tissue and is relying on a certain auto-fluorescence lifetime regime in order to do so. The system can best distinguish auto-fluorescence decay constants between 0.5 to 20 ns. Most abundant fluorophores in tissue have auto-fluorescence in this regime. Identifying fluorophores like FAD and NAD which have multiple sub-nanosecond decay factors, is not easily detectable (Islam et al. 2013). Moreover, proteins that are found in tissue in comparably minute quantities would not contribute to a macroscopic contrast map (above 1 cm^2).

Maximum Permissible Exposure (MPE) is a limit defined by the American National Standard (Z136.1-2007), and sets the safety limits for radiation by definitions of exposure parameters including duration and peak power for the different wavelengths. The contrast based autofluorescence imaging system utilizes the near UV region (300 to 400nm) for illumination of biological specimen without using lasers. The exposure and safety limits for patients and personnel

using this LED based technology allow for comfortable conditions and safe exposures that enable the performance of experiments without harming biological tissues.

Optical imaging for brain tissue characterization using relative fluorescence lifetime imaging

Abstract:

An autofluorescence lifetime wide-field imaging system that can generate contrast in underlying tissue structures of normal and malignant brain tissue samples with video rate acquisition and processing time is presented. Images of the investigated tissues were acquired with high resolution (∼35 μm) using an algorithm to produce contrast based on differences in relative lifetimes. Sufficient contrast for delineation was produced without the computation of fluorescence decay times or Laguerre coefficients. The imaged tissues were sent for histological analysis that confirmed the detected imaged tissues morphological findings and correlations between relative lifetime maps and histology identified.

Keywords: fluorescence; real-time imaging; relative lifetime; ultraviolet; light emitting diodes; brain tumor.

Fluorescence lifetime imaging has demonstrated the ability to accurately detect materials and tissue constituents with robustness to varying yield and emission scattering materials [1–6]. Current fluorescence lifetime systems rely on accurate temporal sampling to capture the tails of the decaying emission. This data is often fit to an exponential decay model or a set of Laguerre polynomials to extract coefficients related to decay times [5–9]. While these methodologies provide powerful tools for material constituent identification they are often implemented as point

measurement systems and require significant post processing to compute decay times and/or coefficients. In some applications these factors can hinder clinical translation.

Based on these observations our group has developed algorithms and system designs that trade away information (explicit extraction of decay times) for improvements to system simplicity and image acquisition time. Contrast is generated by developing spatially resolved maps of relative differences in auto fluorescence decay of tissue constituents. This method uses a gated CCD and diode array and was explored in a previously published paper [1] and the pertinent details are repeated below. The system has accomplished fast acquisition and processing algorithms that allow for a wide field to be acquired simultaneously and may extend the use of this modality to the intraoperative environment [1]. These improvements were enabled by employing light emitting diodes (LED) and long illumination pulse durations to create a detection system capable of imaging wide field of view (FOV) with high resolution while maintaining low peak power and

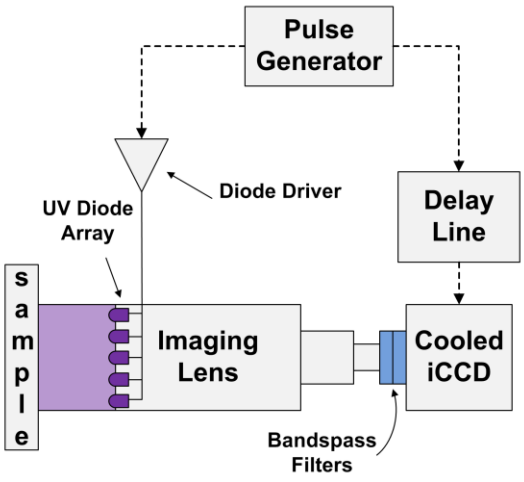

Figure 5. Fluorescence imaging system setup.

avoiding photo bleaching (Figure 5). The resulting image displays a map proportional to the relative lifetime values on a predetermined color scale. This approach ensures very fast processing since only two images are acquired and no de-convolution or lifetime calculations are needed. The system has demonstrated an ability to distinguish between lifetime differences of less than 6% in imaging dyes and powders [1]. We show here for the first time the utility of the system in distinguishing brain tissue morphology and structure followed by histological analysis confirming the contrast mechanism and sensitivity of the system.

This current iteration has undergone numerous upgrades to increase the contrast and ease of operability. Illumination has been modified to a circular aperture mounted with 6 UV-LEDs to ensure more uniformity when imaging rough surfaces. Each LED is rated at 2 mW optical power at 375 nm central wavelength. The LEDs' circuit operates at an average optical power of 2 μW driven by a high voltage pulse generator (Avtech AVR-E2-C) at 0.02% duty cycle. The low duty cycle ensures thermal stability of the LEDs and produces fluence levels five orders of magnitude below the ANSI standard [Z136.1_2007]. A filter mount has been placed in front of the intensified CCD (ICCD) (Andor iStar DH734) to take advantage of the wavelength dependent decay times of tissue constituents. The imaging optic utilized in this experiment was a high numerical aperture SLR macro lens (Canon MP-E 65) which afforded a ~1 cm FOV at a standoff of ~8 cm. With these specifications and the iCCD camera's focal plane array dimensions the practical feature size limit is ~ 35 μm.

A diagram of the operational principles of the algorithm is displayed in Figure 6. The comprehensive acquisition method has been described in Jiang et al. and a concise summary is

described here; the gated intensified camera is set to capture two images, one during the illumination period and the latter during the fluorescence decay period. These two images contain all the information needed to discern between different constituents and eliminate varying yield factors and absorption while being sensitive only to lifetime differences. (Figure 6) Each pixel is normalized to its maximum fluorescence emission (in the calibration image) and hence yield and absorbance do not interfere with lifetime information representation. Software execution of this algorithm involves the pixel wise division of two 1M pixels images in a 16 bit format, and requires a processing time of ~5 ms using MATLAB without any optimizations. Moreover, using this long acquisition method ensures SNR is not the limiting factor for the generation of sufficient contrast

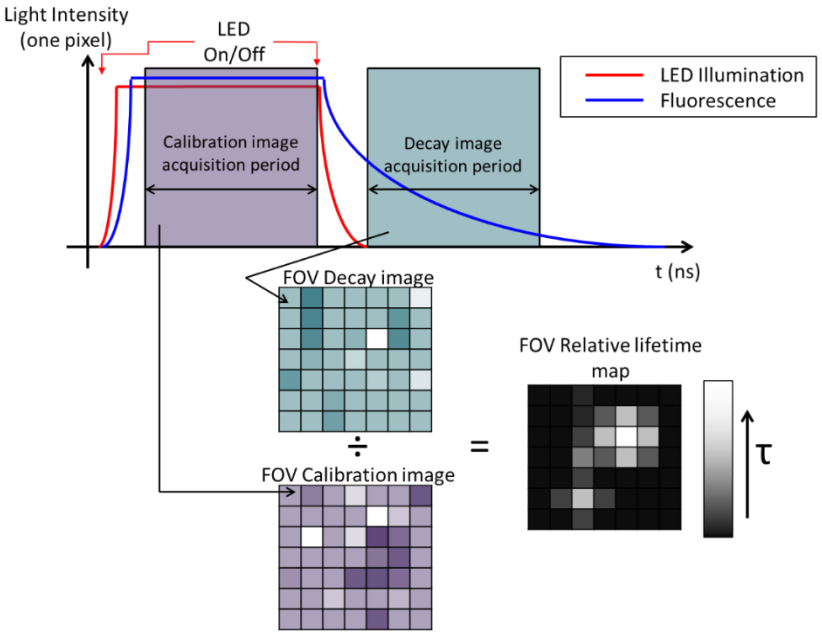

Figure 6. Relative fluorescence lifetime algorithm.

and allows total acquisition of 1 second.

Acquisition methodology: A calibration image is acquired during LED illumination and then saved, CCD resets and the second image – the decay image – is acquired and saved. The decay

image is then divided by the calibration image: Each pixel's intensity value in the decay image is divided with the corresponding pixel in the calibration image, this results in a final relative lifetime image (normalized image). Each pixel is integrating intensity of the fluorescence signal over the acquisition period, hence the advantage of high SNR in our system. Since the fluorophore lifetime and recorded signals are correlated, this algorithm presents only the relative lifetime information, where bright pixels represent longer lifetimes.

Brain tissue samples were selected to test the capabilities of this system to delineate varying tissue pathologies. One frozen glioma sample and one frozen dura mater sample were acquired from the UCLA Brain Tumor Translational Resource (BTTR) and placed on glass microscope slides for imaging. The glioma tissue was from a histologically confirmed glioblastoma WHO Grade IV patient though the sample used for this study showed only infiltrating areas of the glioma without necrosis. The tissue was mounted in OCT and then sliced flat with a cryotome to ensure a flat imaging field. The samples were placed on a cooled stage with temperature controlled thermoelectric cooler to slow the deterioration of tissue at room temperature. Following acquisition, the samples were marked with a standard histology dye for orientation purposes and sent to the BTTR for histologic analysis.

Preparation of the samples for histological analysis included embedding in paraffin while maintaining the desired orientation. In order to achieve maximum information of the tissue surface while maintaining orientation, the samples were sliced vertically, similarly to bread slicing as illustrated in Figure 7 and stained with Hematoxylin and Eosin (H&E) prior to microscopy.

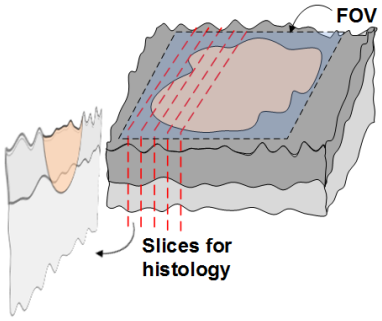

Figure 7. The bread slice loafing employed by the BTTR.

The bread slice method ensures accurate orientation of the sample and image corresponding histological analysis. Samples sectioned vertically to imaging plane for accurate correlations between images and pathology to be stained with H&E for analysis.

Since our system has large sensitivity range (1 MHz readout with 13bit effective dynamic range), good visual contrast is hard to perceive even on modern LCD screens, customization of the image lookup table can mediate that problem (Figure 8 c & d). Choosing an optimized color map (lookup table) to represent relative lifetime values with even higher apparent contrast is being optimized by our group and others [10]. Figure 8 (a) displays gray scale fluorescence intensity (steady state) images of the glioma sample and dura mater (b), high intensity corresponds to brighter pixels. The lifetime images in Figure 8 (c) & (d) are displayed with the color map adjacent to each image, where shorter relative lifetimes are yellow (and blue) and longer relative lifetimes are red.

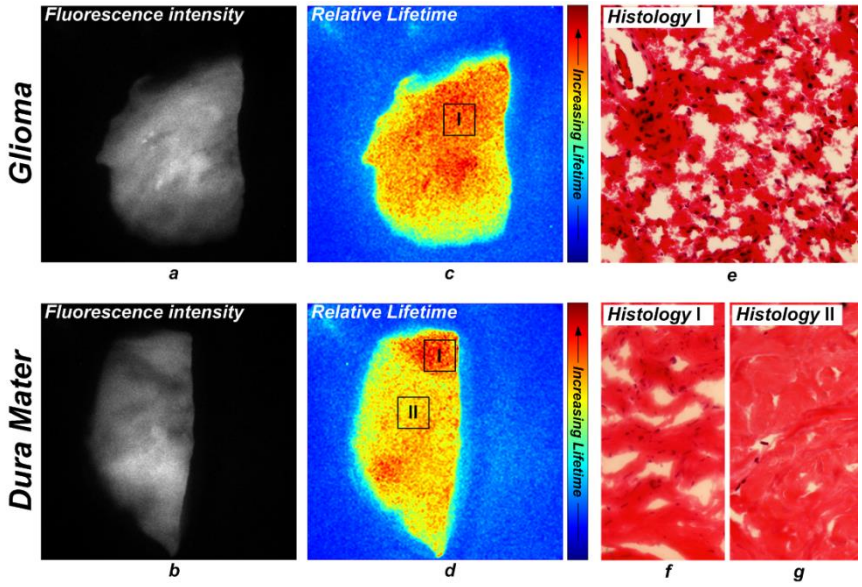

Figure 8. Brain tissue imaging results.

Brain tissue imaging results & analysis: (a) & (b) Fluorescence intensity images of the 'calibration image'. (c) & (d) Custom color map of relative lifetimes: red represents longer lifetime. (e) Histology results of the marked region in (c) showing malignant tissue composition, glioma tissue was relatively uniform hence only one area was tested. (f) & (g) Histology result of marked region I and II, respectively showing in (d). The relative lifetime map was not altered or enhanced other than applying the colormap to pixel's values.

These lifetime images display contrast that is not detectable in the gray scale 'calibration' images (a) & (b) and show fine structure corresponding to tissue morphology. Figure 8 (e) shows a low to moderate cellularity area of neoplastic astrocytes from a glioblastoma patient. Histology of region I is fairly uniform which correlates well with the relative uniformity of the lifetime fluorescence image. Figure 8 (f) & (g) shows histology from 2 distinct regions of a sample of dura

mater. Region I is a relatively cellular area showing multiple nuclei. Region II was relatively devoid of fibroblastic nuclei and consisted mostly of dense collagen. Pathological results correlate with the relative lifetime map and further confirm the system's ability to detect tissues abnormalities. The heterogeneous imaging signals arising from regions I and II may reflect the relative presence or absence of fibroblasts in these areas.

Using relative lifetime normalization methodology to create contrast images has great potential when used in ex vivo samples. The rapid imaging rate and the high contrast generated offers a unique implementation of fluorescence lifetime imaging that carries the potential for intraoperative cancer margin delineation and accurate scission that offers better patient outcome. Those capabilities coupled with modular, low cost components bring closer the realization to implement this system in clinical setting. Ongoing research with a large sample pool to generate significant statistical data is underway.

This work was sponsored by the Telemedicine & Advanced Technology Research Center (TATRC), grant# W81XWH-12-2-0075.

References:

[1] P.-C. Jiang, W. S. Grundfest, and O. M. Stafsudd, "Quasi-real-time fluorescence imaging with lifetime dependent contrast," *J. Biomed. Opt* **16**(8), 086001–086001 (2011) [doi:10.1117/1.3609229].

[2] J. Phipps, Y. Sun, R. Saroufeem, N. Hatami, M. C. Fishbein, and L. Marcu, "Fluorescence lifetime imaging for the characterization of the biochemical composition of atherosclerotic plaques," *Journal of Biomedical Optics* **16**(9), 096018 (2011) [doi:10.1117/1.3626865].

[3] J. E. Phipps, Y. Sun, M. C. Fishbein, and L. Marcu, "A fluorescence lifetime imaging classification method to investigate the collagen to lipid ratio in fibrous caps of atherosclerotic plaque," *Lasers Surg Med* **44**(7), 564–571 (2012) [doi:10.1002/lsm.22059].

[4] Y. Sun, N. Hatami, M. Yee, J. Phipps, D. S. Elson, F. Gorin, R. J. Schrot, and L. Marcu, "Fluorescence lifetime imaging microscopy for brain tumor image-guided surgery," *Journal of Biomedical Optics* **15**(5), 056022 (2010) [doi:10.1117/1.3486612].

[5] J. McGinty, N. P. Galletly, C. Dunsby, I. Munro, D. S. Elson, J. Requejo-Isidro, P. Cohen, R. Ahmad, A. Forsyth, et al., "Wide-field fluorescence lifetime imaging of cancer," *Biomed Opt Express* **1**(2), 627–640 (2010) [doi:10.1364/BOE.1.000627].

[6] J.-M. I. Maarek, L. Marcu, W. J. Snyder, and W. S. Grundfest, "Time-resolved Fluorescence Spectra of Arterial Fluorescent Compounds: Reconstruction with the Laguerre Expansion Technique," *Photochemistry and Photobiology* **71**(2), 178–187 (2000) [doi:10.1562/0031-8655(2000)0710178TRFSOA2.0.CO2].

[7] J. A. Jo, Q. Fang, and L. Marcu, "Ultrafast Method for the Analysis of Fluorescence Lifetime Imaging Microscopy Data Based on the Laguerre Expansion Technique," *IEEE J Quantum Electron* **11**(4), 835–845 (2005) [doi:10.1109/JSTQE.2005.857685].

[8] C. J. de Grauw and H. C. Gerritsen, "Multiple Time-Gate Module for Fluorescence Lifetime Imaging," *Appl. Spectrosc.* **55**(6), 670–678 (2001).

[9] N. p. Galletly, J. McGinty, C. Dunsby, F. Teixeira, J. Requejo-Isidro, I. Munro, D. s. Elson, M. a. a. Neil, A. c. Chu, et al., "Fluorescence lifetime imaging distinguishes basal cell carcinoma from surrounding uninvolved skin," *British Journal of Dermatology* **159**(1), 152–161 (2008) [doi:10.1111/j.1365-2133.2008.08577.x].

[10] C. Stringari, A. Cinquin, O. Cinquin, M. A. Digman, P. J. Donovan, and E. Gratton, "Phasor approach to fluorescence lifetime microscopy distinguishes different metabolic states of germ cells in a live tissue," *PNAS* **108**(33), 13582–13587 (2011) [doi:10.1073/pnas.1108161108].

Ex vivo Retinal Imaging of Porcine Eyes with Preservation of Intraocular Pressure and Shape

Ex vivo retinal imaging can be limited by corneal edema (cloudiness) even in freshly dissected eyes. A method of ex vivo porcine eye retinal imaging is demonstrated by removing the cornea while using exterior optics and a cage assembly, which preserves eye pressure and shape. This method has been used successfully for calibration and feasibility studies during development of a new ophthalmic imaging system in advance of an in vivo human study.

Introduction

The porcine eye is often used as a model eye for retinal research since it exhibits similar properties to the human eye, is readily available and inexpensive. The similar properties include size, cone morphology, and blood vessel configuration (holangiotic retina) [1]. From an optical engineering point of view, the size and shape similarities enable similar focal plane and optical elements.

In some laboratory experiments, *ex vivo* porcine eyes are surface mounted with the cornea facing up. This set up does not lend itself to experimentation with conventional ophthalmic cameras which are designed for a patient sitting upright [2][3]. In these experiments, the entire anterior segment including the cornea, lens, and vitreous are removed in order to get clear images of the retina [4][5]. However, these elements serve as a crucial part of the imaging system and without them the model eye does not represent *in vivo* conditions well.

The main reason for the removal of the cornea, even in freshly harvested porcine eyes, is cloudiness due to corneal edema. Once metabolic processes cease and the eye is harvested, the corneal

endothelium which normally pumps fluid out of the stroma stops working [6][7]. A high hydration level causes disruption in the organization of collagen fibrils, thus reducing transparency and increasing scattering of light [8][9]. (Figure 9).

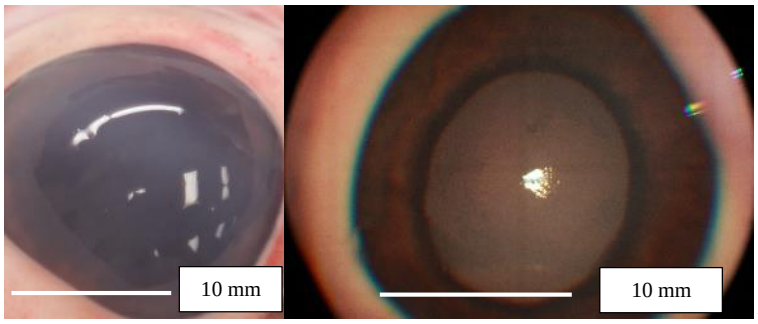

Figure 9. Corneal edema in a porcine eye.

Left: Macro image of the porcine eye using a digital camera (Canon, Rebel T3i) showing corneal edema in ambient light. Right: Higher magnification image using a conventional fundus camera with flash (Zeiss, FF4).

Method

A cage assembly was built to maintain eye pressure and shape while imaging the retina (Figure 10). Porcine eyes were acquired from a slaughterhouse in adherence to the ARVO Statement for the Use of Animals in Ophthalmic and Vision Research. No Institutional Review Board approval was required.

The front holder plate consisted of a cage plate (Thorlabs, CP02, Newton, NJ) with a center bore that was 1" in diameter. A window assembly was made by covering the bore on the outside with a

thin cover glass (Fisher, 12-548-B, Waltham, MA) attached by clear duct tape from all sides creating a leak proof window (Figure 10). This front holder plate with window assembly was then secured to two cage rods that were 1.5 inches long (Thorlabs, ER1.5).

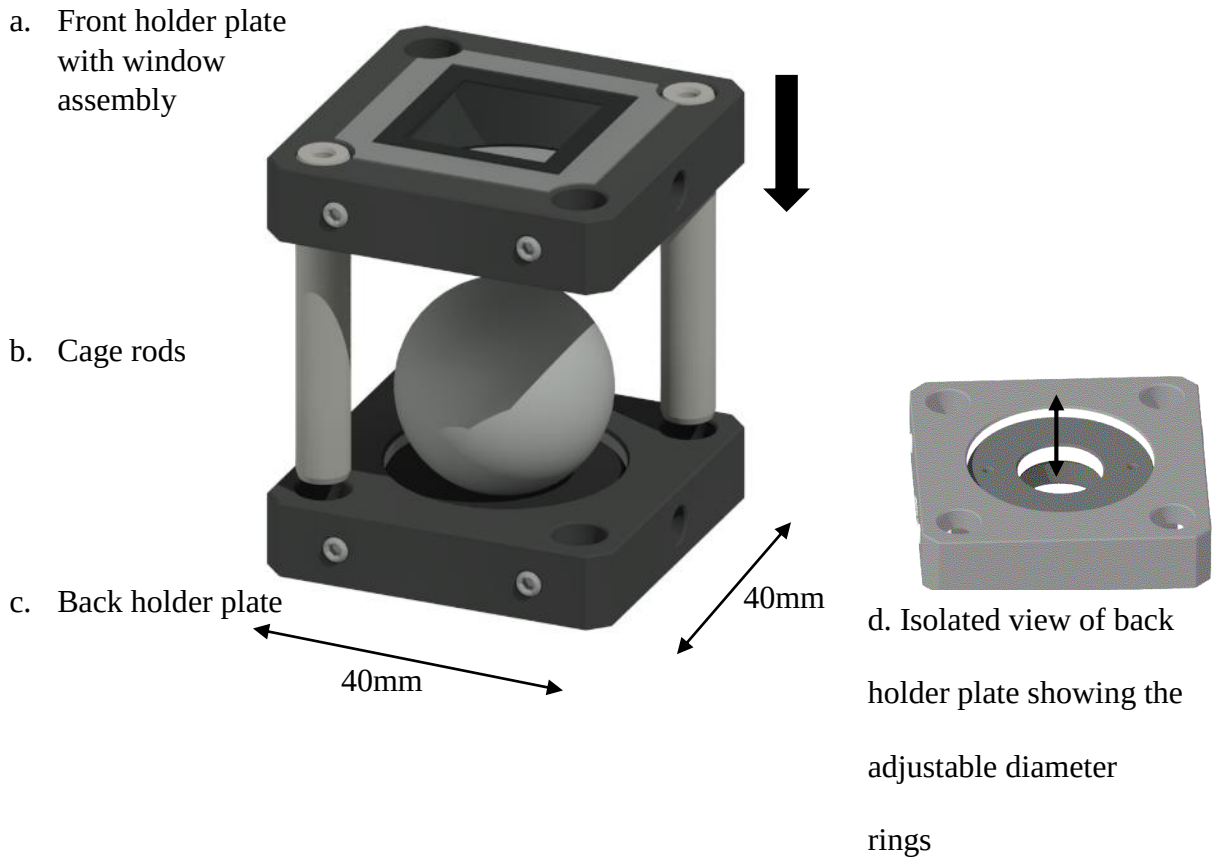

Figure 10. Cage system for ex vivo fundus imaging

Figure 10 (a) Front holder plate with window assembly that enables viewing into the eye. (b) Cage rods secure the eye between the front and back holder plates. (c) Back holder plate supports the posterior surface of the eye. (d) Isolated view of the back holder plate showing the adjustable diameter rings. The spherical surface provides support to prevent retinal stress and can accommodate varying eye sizes.

Cornea removal was performed while the eye was placed on the back holder plate, without the cage rods. The back holder plate included an adjustable inner ring (Thorlabs, S1TM12) with a 0.48 inch radius that nestled the eye in place. This provided center alignment of the eye within the cage assembly and ensured a stable mount for cutting the cornea. In order to avoid damaging the lens in the process, an ophthalmic surgical viscoelastic polymer (Healon, Abbott Medical Optics Inc, Santa Ana, CA) was injected beneath the cornea through a corneal incision.

Once the cornea was removed, the front holder plate with window assembly was pushed down until the anterior segment of the eye was secured by the window assembly (Figure 11. Porcine eye in the windowed cage system). Since some aqueous was lost when removing the cornea, a small amount of saline water (up to 2 cc) was injected with a 30 gauge needle through the pars plana. The eye could then be handled in any position safely. This cage assembly can also be used without the thin cover glass in the case of a healthy cornea or if corneal imaging is desired.

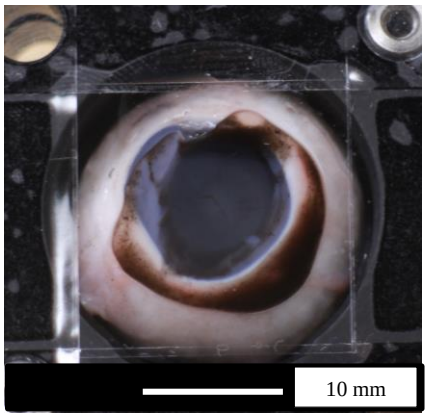

Figure 11. Porcine eye in the windowed cage system

Discussion

It is important to maintain eye pressure and shape in various positions when performing *ex vivo* experiments with ophthalmic cameras designed for an upright patient. Using a cage assembly, this was achieved while preserving the natural environment of the lens and posterior segment and thus avoiding dehydration. .

The adjustable diameter rings on the back holder plate accommodates different eye sizes (15- 30 mm). Suitable animal eyes that can be mounted on the existing cage assembly include monkeys, rabbits and other similarly sized or larger eyes. Larger eyes will benefit from more accurate positioning and intraocular pressure adjustment. In a greater than 30 mm eye, a bigger cage assembly can be made with the same construction design.

The cage assembly was reusable on multiple eyes and able to keep the eyes intact, without leakage or deformation even with repeated use. Moreover, we were able to adjust the eye's orientation inside the cage assembly by shallowly inserting a needle and syringe in the back of the eye and rotating it to the desired optical axis. The cage assembly can be used with tissue fixation procedures when histological analysis is planned. In addition, the cage assembly is made of aluminum and can be cooled to slow tissue degradation by attaching a compact thermo electric cooler (TEC). In case of a long experiment, the caged eye can be readily stored at 4 degrees C overnight and reused the next day.

Testing an ex vivo porcine eye prepared in the cage assembly was performed using a fundus camera (Zeiss, FF4, West Germany) to ensure optical and structural integrity. It was important to keep the lens and vitreous in place to maintain the spectral properties of the eye. The lens and vitreous restrict spectral transparency and limit blue and ultra violet (UV) light from reaching the retina [10][11]. An ex vivo porcine retina, prepared with the proposed procedure, was imaged by adding an external lens that reproduced the cornea's focusing power since most of the eye's refractive power originates from the cornea (approximately 40D) at the tissue-air interface [8] (Figure 12. Cage assembly with added external lens and a color fundus image.).

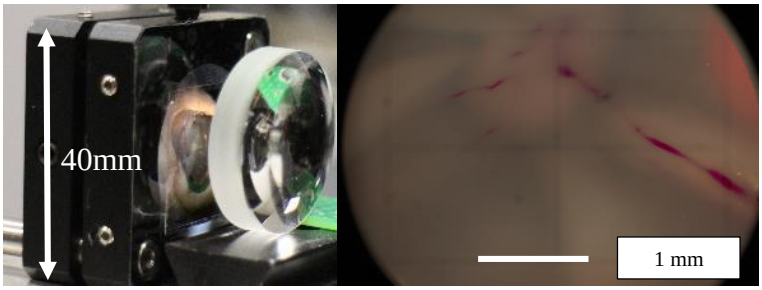

Figure 12. Cage assembly with added external lens and a color fundus image.

A limitation of the cage assembly is that small rodent eyes would be difficult to mount due to the small eye size. In addition, wide angle retinal imaging was restricted due to external lens position.

In summary, ex vivo retinal imaging of porcine eyes with preservation of intraocular pressure and shape was achieved by using inexpensive off the shelf parts to construct a cage assembly. The device can be adapted to various experimental needs.

Acknowledgement

Support of this study was provided by the Stein Eye Institute by donation of equipment.

References

[1] I. Sanchez, R. Martin, F. Ussa, and I. Fernandez-Bueno, “The parameters of the porcine eyeball,” *Graefes Arch. Clin. Exp. Ophthalmol.*, vol. 249, no. 4, pp. 475–482, Apr. 2011.

[2] G. Terauchi, C. S. Matsumoto, K. Shinoda, H. Matsumoto, and A. Mizota, “Effect of Intraocular Lens Diameter Implanted in Enucleated Porcine Eye on Intraocular Pressure Induced by Scleral Depression,” *BioMed Res. Int.*, vol. 2014, p. e586060, Mar. 2014.

[3] K. Y. Chan, P. Cho, and M. Boost, “Corneal epithelial cell viability of an ex vivo porcine eye model,” *Clin. Exp. Optom.*, vol. 97, no. 4, pp. 337–340, 2014.

[4] S. Peters, M. Hammer, and D. Schweitzer, “Two-photon excited fluorescence microscopy application for ex vivo investigation of ocular fundus samples,” 2011, vol. 8086, pp. 808605–808605–10.

[5] K. Kobuch, W. A. Herrmann, C. Framme, H. G. Sachs, V.-P. Gabel, and J. Hillenkamp, “Maintenance of adult porcine retina and retinal pigment epithelium in perfusion culture: Characterisation of an organotypic in vitro model,” *Exp. Eye Res.*, vol. 86, no. 4, pp. 661–668, Apr. 2008.

[6] D. M. Maurice, “The structure and transparency of the cornea,” *J. Physiol.*, vol. 136, no. 2, pp. 263–286.1, Apr. 1957.

[7] K. M. Meek, “The Cornea and Sclera,” in *Collagen*, P. Fratzl, Ed. Springer US, 2008, pp. 359–396.

[8] G. B. Benedek, “Theory of Transparency of the Eye,” *Appl. Opt.*, vol. 10, no. 3, pp. 459–473, Mar. 1971.

[9] Y. M. Michelacci, “Collagens and proteoglycans of the corneal extracellular matrix,” *Braz. J. Med. Biol. Res.*, vol. 36, no. 8, pp. 1037–1046, Aug. 2003.

[10] E. A. Boettner and J. R. Wolter, “Transmission of the Ocular Media,” *Invest. Ophthalmol. Vis. Sci.*, vol. 1, no. 6, pp. 776–783, Dec. 1962.

[11] D. Schweitzer, S. Jentsch, S. Schenke, M. Hammer, C. Biskup, and E. Gaillard, “Spectral and time-resolved studies on ocular structures,” 2007, vol. 6628, pp. 662807–662807–12.

Imaging auto-fluorescence temporal signatures of the human ocular fundus in vivo

Abstract: We demonstrate real time in vivo fundus imaging capabilities of our fluorescence lifetime imaging technology for the first time. This implementation of lifetime imaging uses Light Emitting Diodes (LEDs) to capture full-field images capable of showing direct tissue contrast without executing curve fitting or lifetime calculations. Preliminary results of fundus images are presented, investigating autofluorescence imaging potential of various retina biomarkers for early detection of macular diseases.

Keywords: Fluorescence lifetime Imaging Microscopy; real-time imaging; retina.

Fluorescence Lifetime Imaging Microscopy (FLIM) is a robust imaging modality that has been proven to be sensitive in the detection of chemicals and molecular species in cluttered environments [1–3]. Examples specific to biomedical imaging are the detection of cancerous tumors [4,5] and metabolic changes in the human fundus, aimed to characterize and provide better disease prognosis. Research efforts in the field reported various fluorescence biomarkers and structural contrast mechanisms to investigate detection capabilities for Age-related Macular Degeneration (AMD), diabetic retinopathy, and more [6–12]. These systems utilize point detection by raster scanning and results in long acquisition and processing times. Our group has developed a new imaging method utilizing autofluorescence temporal signatures to test the efficacy of a direct image contrast in various tissues. This technique does not require setting a priori assumptions on

the fluorescence decay behavior and displays lifetime contrast map based on relative changes in lifetime (Figure 13. Relative fluorescence lifetime algorithm.). The contrast image, can be acquired and processed in less than a second [5,13,14]. In this letter we demonstrate the system's capability in imaging full-field human fundus with low excitation fluence, and show structural variations in vivo.

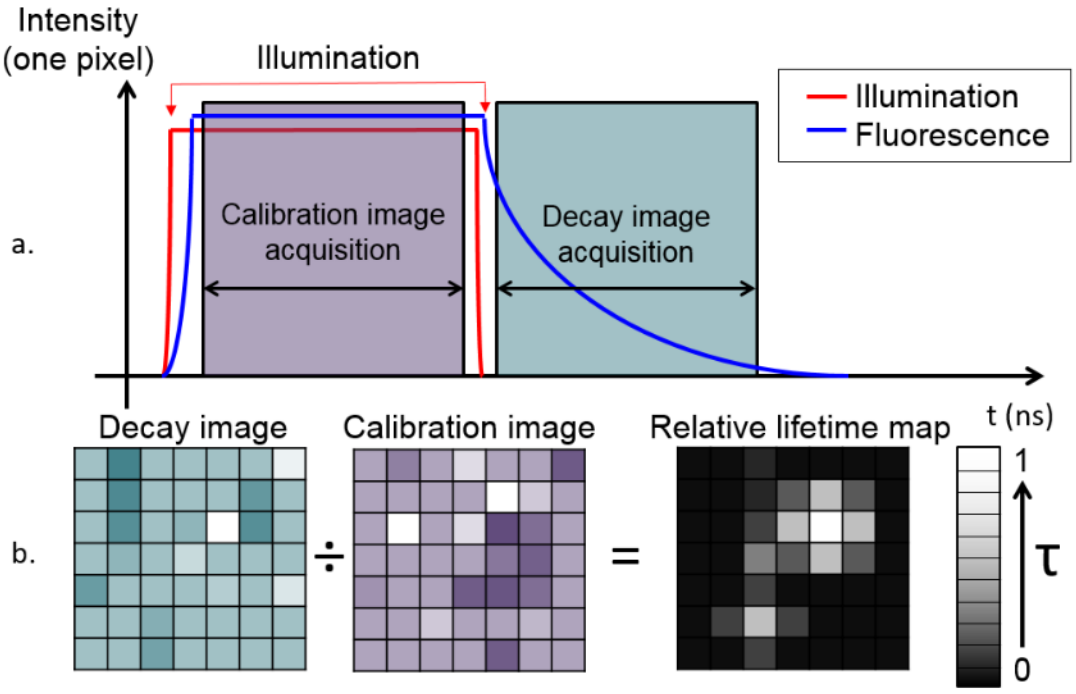

Figure 13. Relative fluorescence lifetime algorithm.

Relative fluorescent lifetime algorithm introduces both hardware and software modifications to the FLIM modality to produce a contrast image: (a) Acquisition of only two images are necessary; one during illumination (calibration image) and the second during fluorescence decay (decay image). Each image is acquired by accumulation of many repetitive pulses by the gated camera to achieve adequate signal level. (b) The decay image is divided by the calibration image using pixel

division and results in a final relative (normalized) lifetime image. High signal levels can be achieved since the fluorescence intensity is recorded over relatively long acquisition period (10 – 20 ns) and with good camera gating efficiency (> 90%). Since the fluorophore lifetime and recorded signals are correlated, this algorithm produces lifetime contrast information without dependency on yield or concentration factors.

System and methods

The illumination scheme in the system relies on a wide field illumination by a diffused LED light providing excitation at 407 nm. Using this wavelength in imaging the retina is possible in pseudophakic patients as the intraocular lens efficiently transmits blue wavelengths and assists in reducing the autofluorescence signal found in crystalline lenses [15,16]. Blue wavelengths have also been reported to excite efficiently metabolic fluorophores such as flavin adenine dinucleotide (FAD) and lipofuscin, among other fluorophores in the retina and pigment epithelium (RPE), with strong signals from structural fluorophores; collagen and elastin [12,17–19]. These signals exhibit broad fluorescence emission spectrum that can be imaged using our detection scheme and potentially used to detect structural and metabolic changes in the retina. The system was built on an existing fundus camera (Zeiss, FF4), that uses conventional optics (not confocal) with an indirect illumination scheme to record color images and fluorescein angiographs from a human retina. Modifications were made to enable imaging of the retina's autofluorescence signals (Figure

14. Modified fundus camera) and include an intensified CCD (ICCD) imager (Andor, iStar 334T) and an LED (Thorlabs, LED405E) set to emit 20 ns long square pulses with 407 nm wavelength and average power of 4 μW at the cornea. Utilizing a blue wavelength with low power levels and flat-top pulses with low average and peak power has been found safe both by the ANSI standard for ocular exposure [20, 21] and reported DNA damage threshold statistics [22]. The LED light passes through two Ultraviolet (UV) optical filters (Thorlabs, FEL0400) to ensure no residual UV light reaches the imaged eye. Another filter is positioned in front of the ICCD to block reflected light and record fluorescence signals from the retina at a central wavelength of 460 nm and 60 nm bandwidth (Semrock, FF01-460/60-25). A high power pulse generator (Avtech, AVR-E3-B-P) drives the LED and triggers the camera operation. The relatively low duty cycle (<0.2%) and the LED impedance matching network ensures optical output without damaging the LED and maintains wavelength stability for extended periods.

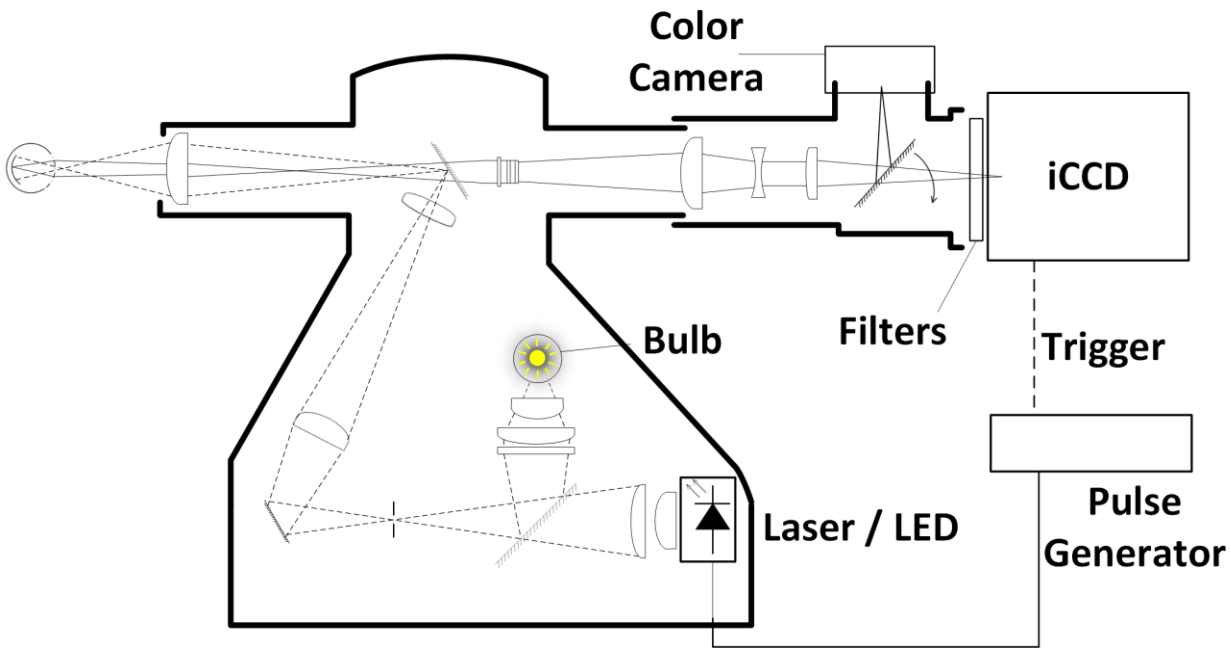

Figure 14. Modified fundus camera

Modified fundus camera schematics: LED and an ICCD are set to generate and capture nanosecond autofluorescence signals from the retina. The LED replaces a xenon flash bulb and the ICCD replaces a conventional CCD module, both used in traditional angiography procedures. Images captured by pulsing the LED and synchronizing the ICCD by the pulse generator. The ICCD is capable of intensifying and imaging the signals to provide full-field images without raster scanning in real time.

Results and discussion

Ex vivo porcine eyes were used as a calibration model for the camera before in vivo experiments were performed as they exhibit similar properties to the human eye. Six fresh eyes, kept in ice to slow tissue deterioration and delivered within two hours of harvesting, were acquired from a local slaughterhouse in adherence to the ARVO Statement for the Use of Animals in Ophthalmic and Vision Research. No Institutional Review Board approval was required. The chosen excitation wavelength transmits through the intraocular structures i.e. lens and vitreous, and excites the retina and blood vessels (Figure 15. ex vivo porcine eye imaging using fundus camera.).

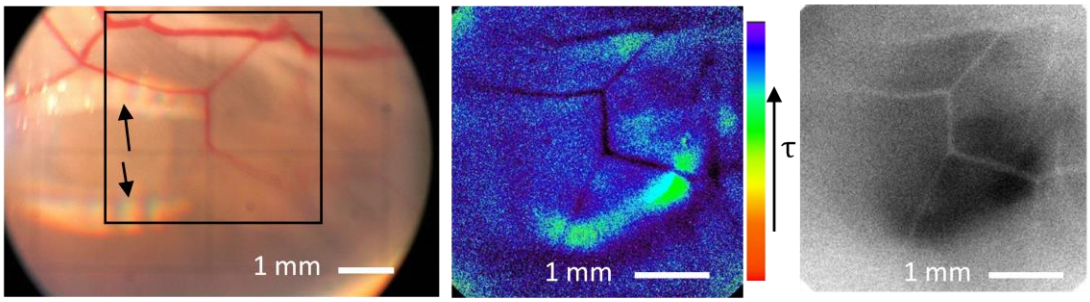

Figure 15. ex vivo porcine eye imaging using fundus camera.

Left: Color fundus image, square represents field of view of the fluorescence images, black arrows point at reflections. Middle: Color threshold autofluorescence relative lifetime image. Right: Grey scale threshold autofluorescence relative lifetime contrast image.

All of the porcine eyes resulted in low detail images due to various degrees of corneal edema (high hydration levels that causes opaqueness). Contrast in these images originates primarily from lifetime difference between blood vessels and retinal connective tissue fluorophores; collagen and elastin. Contribution of the lens' strong autofluorescence signal could explain variations in contrast [17].

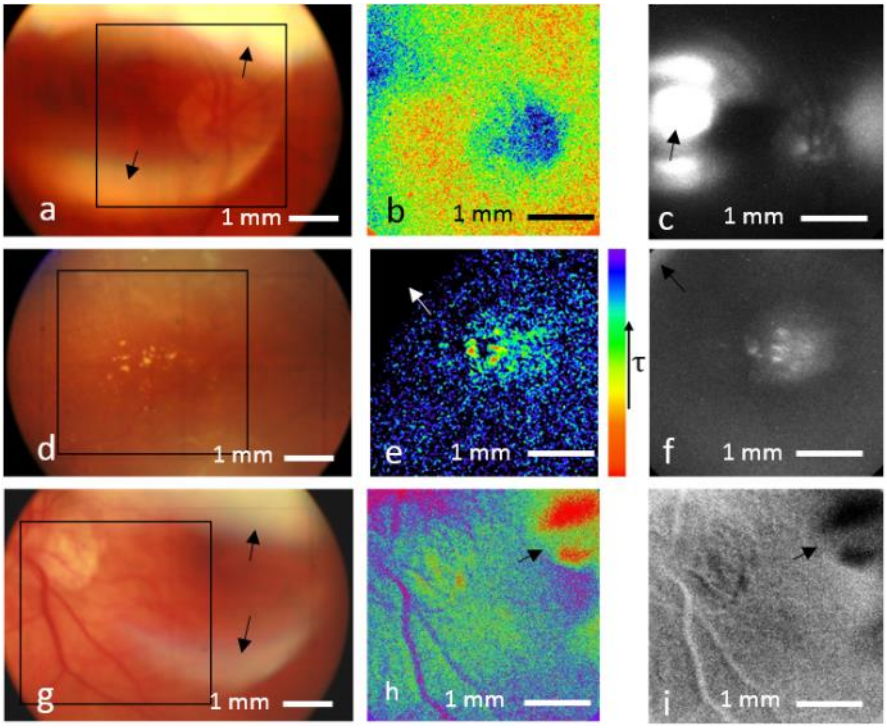

Figure 16. Fundus images of 3 patients.

Color fundus photos of the 3 patients (Figure 16), individual color threshold was set for each image to enhance contrast. Each row represents a single eye measurement, squares in (a,d,g) represent the field of view of the fluorescence images. (b,e,h) are fluorescence lifetime contrast images, (c,f,i) are fluorescence greyscale intensity images. Arrows point at reflections artifacts (common

in pseudophakic patients). Image c and b taken at different times (image b has no reflection artifact).

The in vivo imaging experiment included six pseudophakic volunteer patients from the Stein Eye Institute at UCLA. The experiment was approved by the Internal Review Board (IRB) for human subjects. Three out of the six patients were imaged successfully during system optimization and operator training. Two of the patients were diagnosed with dry AMD (Figure 16 a-c, g-i) and one patient with diabetic retinopathy (Figure 16 d-f). Images of the diabetic patient show low signal levels and bright spots (hyper-fluorescence) of macular edema23. The fluorescence intensity map shows better contrast than the lifetime data and more data is needed in order to validate possible imaging utility for this condition. The first AMD patient (Figure 16 a-c) display high noise level, though basic lifetime contrast between the optic disk and the surrounding retina is visible. Figure 16 (4.b) and (4.c) were taken at different times. Images of the second AMD patient (Figure 16 g-i) exhibit higher detail level and contrast due to optics optimizations. Lifetime image (Figure 16 h) shows signals of the optic disk and blood vessels' margins generated mainly from connective tissue fluorophores. Longer lifetime values in the fovea region is also visible and correlate to previously reported lifetime changes in AMD patients [24]. However, more patient data is needed in order to demonstrate reproducibility and statistical significance. The current fundus camera was not designed for lifetime imaging and has low photon efficiency, though basic fluorescence lifetime data displayed show the robustness of the technique. Diagnosis of AMD, specifically lipofuscin distribution, could possibly be achieved with a modern fundus imager that has higher photon efficiency and reduced reflections.

Conclusions

We have shown a proof of concept of our technique in imaging retina autofluorescence lifetime signatures. Implementation of this imaging method on a modern fundus camera could offer an alternative to existing technologies, using fast fundus imaging without raster scanning. Further improvement of the illumination pulse profile and algorithm optimizations could extract more information and increase signal to noise ratio. Implementation of multi-spectral excitation schemes in future research efforts could also provide better discrimination and contrast of endogenous fluorophores to detect metabolic processes and morphological changes in point of care macular diagnosis.

Acknowledgments

This work was sponsored by the Telemedicine & Advanced Technology Research Center (TATRC), grant# W81XWH-12-2-0075. Support of this study was provided by the Stein Eye Institute by donation of equipment. Imaging of patients were approved by UCLA institutional review board, IRB 14-000767.

References

1. N. Mazumder et al., “Fluorescence Lifetime Imaging of Alterations to Cellular Metabolism by Domain 2 of the Hepatitis C Virus Core Protein,” PLoS ONE **8**(6), e66738 (2013) [doi:10.1371/journal.pone.0066738].
2. T. S. Blacker et al., “Separating NADH and NADPH fluorescence in live cells and tissues using FLIM,” Nat. Commun. **5** (2014) [doi:10.1038/ncomms4936].
3. J.-M. I. Maarek et al., “Time-resolved Fluorescence Spectra of Arterial Fluorescent Compounds: Reconstruction with the Laguerre Expansion Technique,” Photochem. Photobiol. **71**(2), 178–187 (2000) [doi:10.1562/0031-8655(2000)0710178TRFSOA2.0.CO2].
4. Y. Sun et al., “Fluorescence lifetime imaging microscopy for brain tumor image-guided surgery,” J. Biomed. Opt. **15**(5), 056022 (2010) [doi:10.1117/1.3486612].
5. A. Papour et al., “Optical imaging for brain tissue characterization using relative fluorescence lifetime imaging,” J. Biomed. Opt. **18**(6), 060504–060504 (2013) [doi:10.1117/1.JBO.18.6.060504].
6. M. Hammer et al., “In vivo and in vitro investigations of retinal fluorophores in age-related macular degeneration by fluorescence lifetime imaging,” 2009, 71832S – 71832S – 12 [doi:10.1117/12.807943].

7. D. Schweitzer et al., “Fluorescence lifetime imaging ophthalmoscopy in type 2 diabetic patients who have no signs of diabetic retinopathy,” J. Biomed. Opt. **20**(6), 61106 (2015) [doi:10.1117/1.JBO.20.6.061106].
8. C. Dysli, S. Wolf, and M. S. Zinkernagel, “Fluorescence Lifetime Imaging in Retinal Artery Occlusion,” Investig. Opthalmology Vis. Sci. **56**(5), 3329 (2015) [doi:10.1167/iovs.14-16203].
9. C. Dysli et al., “Quantitative Analysis of Fluorescence Lifetime Measurements of the Macula Using the Fluorescence Lifetime Imaging Ophthalmoscope in Healthy Subjects,” Invest. Ophthalmol. Vis. Sci. **55**(4), 2106–2113 (2014) [doi:10.1167/iovs.13-13627].
10. A. von Rückmann, F. W. Fitzke, and A. C. Bird, “Fundus autofluorescence in age-related macular disease imaged with a laser scanning ophthalmoscope.,” Invest. Ophthalmol. Vis. Sci. **38**(2), 478–486 (1997).
11. D. Schweitzer et al., “Evaluation of time-resolved autofluorescence images of the ocular fundus,” 9 October 2003, 8–17 [doi:10.1117/12.499641].
12. M. Islam et al., “pH Dependence of the Fluorescence Lifetime of FAD in Solution and in Cells,” Int. J. Mol. Sci. **14**(1), 1952–1963 (2013) [doi:10.3390/ijms14011952].
13. P.-C. Jiang, W. S. Grundfest, and O. M. Stafsudd, “Quasi-real-time fluorescence imaging with lifetime dependent contrast,” J. Biomed. Opt. **16**(8), 086001–086001 (2011) [doi:10.1117/1.3609229].
14. A. J. Sherman et al., “Normalized fluorescence lifetime imaging for tumor identification and margin delineation,” Proc SPIE 8572 Advanced Biomedical and Clinical Diagnostic Systems XI, 85721H – 85721H (2013) [doi:10.1117/12.2013414].

15. J. A. Zuclich et al., “Near-UV/blue light-induced fluorescence in the human lens: potential interference with visual function,” J. Biomed. Opt. **10**(4), 044021–044021 – 7 (2005) [doi:10.1117/1.1990163].
16. E. A. Boettner and J. R. Wolter, “Transmission of the Ocular Media,” Invest. Ophthalmol. Vis. Sci. **1**(6), 776–783 (1962).
17. D. Schweitzer et al., “Spectral and time-resolved studies on ocular structures,” 2007, 662807–662807 – 12 [doi:10.1117/12.726701].
18. A. D. Marmorstein et al., “Spectral Profiling of Autofluorescence Associated with Lipofuscin, Bruch’s Membrane, and Sub-RPE Deposits in Normal and AMD Eyes,” Invest. Ophthalmol. Vis. Sci. **43**(7), 2435–2441 (2002).
19. J. R. Sparrow et al., “A2E, a Lipofuscin Fluorophore, in Human Retinal Pigmented Epithelial Cells in Culture,” Invest. Ophthalmol. Vis. Sci. **40**(12), 2988–2995 (1999).
20. Laser Institute of America, “American National Standard for the safe use of laser ANSI Z 136.1-2007.”
21. F. C. Delori, R. H. Webb, and D. H. Sliney, “Maximum permissible exposures for ocular safety (ANSI 2000), with emphasis on ophthalmic devices,” J. Opt. Soc. Am. A **24**(5), 1250–1265 (2007) [doi:10.1364/JOSAA.24.001250].
22. R. P. Sinha and D.-P. Häder, “UV-induced DNA damage and repair: a review,” Photochem. Photobiol. Sci. **1**(4), 225–236 (2002) [doi:10.1039/B201230H].
23. A. Pece et al., “Autofluorescence Imaging of Cystoid Macular Edema in Diabetic Retinopathy,” Ophthalmologica **224**(4), 230–235 (2010) [doi:10.1159/000260229].

24. D. Schweitzer et al., “In vivo measurement of time-resolved autofluorescence at the human fundus,” J. Biomed. Opt. **9**(6), 1214–1222 (2004) [doi:10.1117/1.1806833].

Raman Stokes scattering background

The Raman Effect is an inelastic optical scattering phenomena that can reveal materials' chemical information. The Raman spectra of a material is sensitive to specific chemical bonds and serves as an optical fingerprint identifying chemical composition (Figure 17).

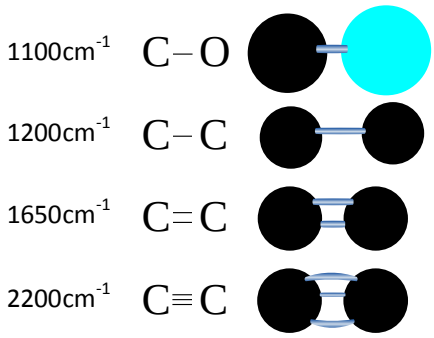

Figure 17. Molecular scattering energies correspond to mass and bond's strength

Light scattered by the Raman Stokes mechanism (Figure 18), is red-shifted due to energy absorption of the molecule. The absorbed amount corresponds to molecular vibrational states of the bond. These vibrational states are well defined and are restricted to allowed vibrational modes corresponding to an harmonic motion and can be approximated by Newtonian mechanics and by Quantum mechanics; defining selection rules of the quantum number $\Delta n = \pm 1$. The observation of the specific vibrational modes creates an accurate detection of molecular species making Raman modality an alluring technique in biology due to its high specificity.

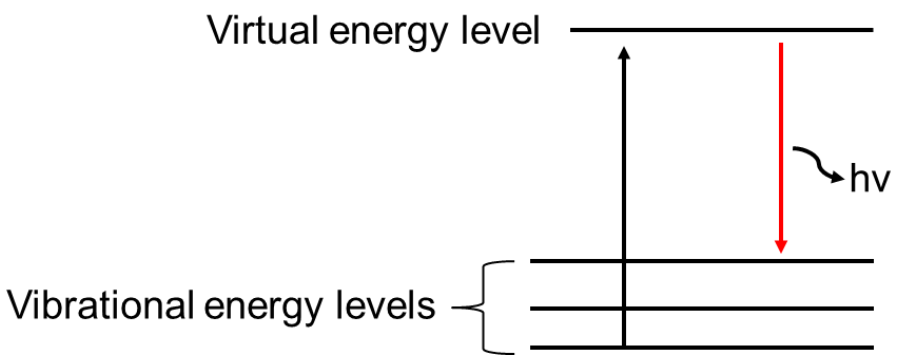

Figure 18. Raman Stokes scattering

Practically, a monochromatic light is scattered by (elastic) Rayleigh scattering and a small fraction, depending on the incident wavelength and Raman cross section (among other factors), is Raman shifted to create a spectrum of the allowed vibrational states of the molecule. This spectrum displays the Raman shift in wavenumbers (cm^{-1}) to represent absolute energy values, independent of the excitation wavelength. This Raman shift can be calculated by the excitation (λ_0) and Raman (λ_1) wavelengths in nanometers (nm) using Eq. 6:

$$\Delta\lambda(cm^{-1}) = \left(\frac{1}{\lambda_0(nm)} - \frac{1}{\lambda_1(nm)}\right) \cdot 10^7$$

By comparing the Raman spectrum of known materials' signature, a match is found and the molecular structure is identified.

This technique requires point measurement that encapsulates a two dimensional Raman spectra. Raster scanning an area to produce a Raman map requires identification of each point's spectra and false-color each material/pixel to create a contrast map. This approach is very accurate but requires long scanning time due to the low Raman signal, and/or, high fluence levels to produce

more Stokes Raman photons. In biological application, especially in *in vivo* large field of view (>1 cm^2) imaging area, long scanning time becomes non-practical and high illumination levels are restricted by Maximum Permissible Exposure (MPE) standards set by the ANSI safety code. Several approaches to Raman imaging have been developed, in part to increase the Raman signals. The following section presents several different Raman approaches and explores the potential of these systems for *in vivo* imaging.

Raman imaging systems comparison

Comparison of Raman imaging systems is displayed in the white-space chart (Figure 19) below:

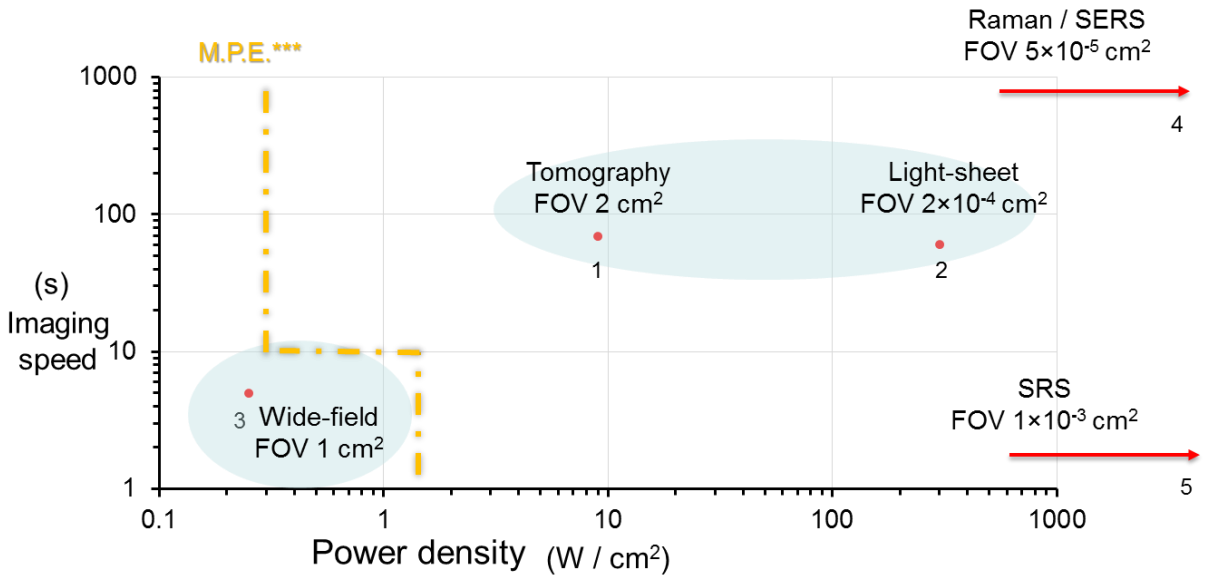

Figure 19. Raman systems performance comparison

The five systems in the chart represent different methodologies for Raman imaging, each utilizes a different excitation scheme.

1. Demers, J.-L. H., Esmonde-White, F. W. L., Esmonde-White, K. A., Morris, M. D. & Pogue, B. W. Next-generation Raman tomography instrument for non-invasive in vivo bone imaging. Biomed. Opt. Express **6**, 793–806 (2015).
2. Y. Oshima, H. Sato, H. Kajiura-Kobayashi, T. Kimura, K. Naruse, and S. Nonaka, "Light sheet-excited spontaneous Raman imaging of a living fish by optical sectioning in a wide field Raman microscope," Opt. Express **20**, 16195 (2012).
3. A. Papour, J. H. Kwak, Z. Taylor, B. Wu, O. Stafsudd, W. Grundfest, "Wide-field Raman imaging for bone detection in tissue," ACCEPTED, Biomed. Opt. Express 2015.
4. A. F. Palonpon, J. Ando, H. Yamakoshi, K. Dodo, M. Sodeoka, S. Kawata, and K. Fujita, "Raman and SERS microscopy for molecular imaging of live cells," Nat. Protoc. **8**, 677–692 (2013).
5. M. Ji, D. A. Orringer, C. W. Freudiger, S. Ramkissoon, X. Liu, D. Lau, A. J. Golby, I. Norton, M. Hayashi, N. Y. R. Agar, G. S. Young, C. Spino, S. Santagata, S. Camelo-Piragua, K. L. Ligon, O. Sagher, and X. S. Xie, "Rapid, Label-Free Detection of Brain Tumors with Stimulated Raman Scattering Microscopy," Sci. Transl. Med. 5, 201ra119–201ra119 (2013).

The Tomographic system (Ref. #1) exhibits the largest field of view of all systems. The resulting cross sectional image is beneficial in small animal models studies and utilizes Raman stokes scattering for in-depth tissue imaging. Despite these advantages, the long imaging times, the illumination and detection assembly, and the high fluence levels (above the MPE), this device is not translatable to human applications. Raman stokes scattering coupled with the light-sheet illumination scheme (Ref. #2), is a microscopic imaging system that illuminates the field of view with a flat illumination beam. The small field of view coupled with a non-trivial beam shape limits the use of this technology. The Stimulated Raman Scattering - SRS (Ref. #5) and Surface Enhanced Raman Scattering - SERS (Ref. #4) systems show good imaging capabilities, however, as in the light-sheet system, they are limited to a microscopic approach with a small field of view, and high illumination power due to the weak nature of Raman scattering. Moreover, these systems do not have the capability to image deep in tissue (1 cm); SERS only enhances (surface) signals that are in contact with the Raman enhancing chemical/particle, while SRS relies on illuminating the sample with two laser beams, a condition that has limited feasibility in deep-tissue imaging or other turbid medium.

The Wide-field system (Ref. #3), developed in our lab, was designed for human *in vivo* application with high photon efficiency and target-oriented imaging performance. This system is designed to answer an unmet clinical need for bone detection in tissue. Targeting a specific application removes many hurdles in utilizing Raman imaging in patient care.

Detailed system configuration and preliminary results are presented in the following chapter.

*** The MPE exhibited in the chart is comprised of two regions; exposure durations of 10^{-7} to 10^{1} seconds, and durations of 10^{1} to 3×10^{4} seconds. These limits are valid for systems 1, 2 and 3. Systems 4 and 5 have different safety limits, nonetheless they operate above the MPE.

Wide-field Raman imaging for bone detection in tissue

Abstract:

Inappropriate bone growth in soft tissue can occur after trauma to a limb and can cause a disruption to the healing process. This is known as Heterotopic Ossification (HO) in which regions in the tissue start to mineralize and form microscopic bone-like structures. These structures continue to calcify and develop into large, non-functional bony masses that cause pain, limit limb movement, and expose the tissue to reoccurring infections; in the case of open wounds this can lead to amputation as a result of a failed wound. Both Magnetic Resonance Imaging (MRI) and X-ray imaging have poor sensitivity and specificity for the detection of HO, thus delaying therapy and leading to poor patient outcomes. We present a low-power, fast (1 frame per second) optical Raman imaging system with a large field of view (1 cm^2) that can differentiate bone tissue from soft tissue without spectroscopy, this in contrast to conventional Raman microscopy systems. This

capability may allow for the development of instrumentation which permits bedside diagnosis of HO.

Keywords: Scattering, Raman; Medical and biological imaging; Tissue characterization.

Introduction

Biocompatible Raman imaging of tissue, particularly imaging of tissue in vivo, has not yet translated to the clinical setting for several reasons. Most Raman techniques are time-consuming, require expensive and bulky systems, and are destructive in nature due to large illumination fluence [1–3]. There exist many disorders that cannot be detected or imaged via traditional methods and could use the high specificity that Raman signals offer. The detection of bone tissue that forms outside the skeleton is hypothetically an ideal candidate disorder, as the Phosphorus-Oxygen bond provides a strong, unique Raman signature [1–4]. This mineralization growth occurs in traumatic wounds of the limbs where the injury affects soft tissue and is prevalent in combat wounds [5–8]. HO also arises in spinal injuries, severe burns and in the surgical beds resulting from orthopedic surgery complications [1,6,9,10]. The biochemical and physiologic mechanisms surrounding HO are not well understood and many precursors of HO are often poor predictors of the eventual establishment of HO, e.g. not all detectable fibrous abnormalities lead to HO [5,8]. In failed

wounds in the extremities (limbs), bone growth is impossible to detect in the early stages and treatment includes resection of the ossified (mineralized) areas and topical or intravenous delivery of medications. The delayed detection followed by late treatment can lead to amputation to avoid potentially life threatening infection [4]. While early detection is crucial, current technologies including X-ray (CT) and Magnetic Resonance Imaging (MRI), are limited and do not offer the resolution and specificity that is required in HO detection. Typical resolution limit for a CT scan is about 1 mm [11] however these scans are not practical for daily patient monitoring due to high costs and, most importantly, high levels of ionizing radiation [12]. There is a clinical need for imaging techniques capable of providing fast, inexpensive, in vivo detection at a stage early enough to allow for appropriate treatment. Several research efforts employ multi-point tomographic imaging schemes for bone detection [13,14], while others use wide-field illumination and acquisition methods [15,16], yet no commercial imaging devices are currently available in the clinical setting. Traditional Raman systems involve point measurement and acquisition of Raman spectra using a spectrometer. The spectra obtained from such an acquisition procedure are then compared to a known spectral database to find a match. These spectra can serve as a fingerprint to identify elements of a sample and, in the case of medical diagnostics, the constituents of tissue. In spectrometer based methodologies, detection is performed by raster scanning the sample area point by point and then coloring techniques are used to create contrast maps corresponding to the spatial location of particular constituents. This method is very specific; however, it is a time-consuming process that cannot be easily applied in vivo [17,18]. Two prominent problems are artifacts caused by the natural movements of the patients, and high fluence levels of the illumination source. Moreover, this methodology does not scale efficiently into imaging a large field of view of 0.1

cm^2 and above. Since stokes-Raman scattering exhibits low signal levels due to small cross section, a powerful laser source or a focused beam is required in order to generate a detectable signal. High fluence levels can cause dehydration of the tissue, denaturation of proteins, and destruction of other constituents and is limited in in vivo tissue imaging by the Maximum Permissible Exposure (MPE) set by ANSI safety code [Z136.1-2007]. Broad fluorescence emission impose another difficulty in recording Raman signals and often requires photo-bleaching or extremely complicated laser systems to generate a 'cleaner' Raman signal [19]. Stokes Raman signals are several orders of magnitude weaker than fluorescence signals and several methods have been developed to amplify Raman signals, amongst them are stimulated themes such as Coherent Anti-stokes Raman Scattering (CARS) and Stimulated Raman Scattering (SRS) [20]. Clinical acceptance of these methods has not been proven due to the need for establishing a coherent illumination condition and the requirement of expensive and bulky laser systems. These patient sampling and biocompatibility issues indicate that traditional Raman techniques, though of extreme utility for in vitro or ex vivo settings, are currently not practical for in vivo or translational research applications.

Methods

The system was built around an 852 nm tunable narrow-band optical filter (Semrock, LL01-852-25) with 3 nm bandwidth (full-width half-maximum) mounted in front of the imaging optics and

serves as the Raman band differentiator (Figure 20). The tested imaging sensors were: Intensified CCD (ICCD) camera (Andor, iStar 334T) and Near Infra-Red (NIR) CCD camera (Andor, iKon-M 934). Both cameras were equipped with a 1 mega-pixel CCD sensor and provide 1 cm field of view, attained by a wide aperture macro lens (Canon, MP-E 65 mm). Diode laser illumination (Thorlabs, L785P090) supplies 90 mW power at 785 nm with ~1.4 nm bandwidth. Additional optical filters were encased in the detection optics platform to block light that falls outside the detection band: 785 nm notch filter (Semrock, NF03-785E-25), and a bandpass filter at 842 nm (Semrock, FF01-842/56-25) central wavelength with 30 nm spectral bandwidth (full-width half-maximum). The laser beam was defocused using an aspheric lens (Thorlabs, C280TME-B) and offered an illumination area of 30 mm^2 at a power density of 250 mW/cm^2, well below the MPE. The narrow band optical filter enables sensitive selection of the incoming signal from 849 to 852 nm. Tuning the narrow-band filter is done by changing the angle in which it is positioned in relation to the optical axis. Through angular adjustment, a multi spectral selection is achieved for each recorded image: 852 nm central wavelength at 0 degrees, to 849 nm at 10 degrees rotation. A pivot filter holder (Thorlabs, CP360R) was customized and coupled to a translation stage assembly for accurate rotation control. Rotation parameters of the filter were set upon calibration using a broad-band NIR LED source and a spectrometer (Ocean Optics, HR4000CG-UV-NIR). The final Raman map is computed by subtraction of two images (Figure 21): First image captures the unique Raman stokes signal of the phosphate symmetric stretch at 960 cm^{-1}, and the second image captures only fluorescence and background signals of the tissue at 1002 cm^{-1}.

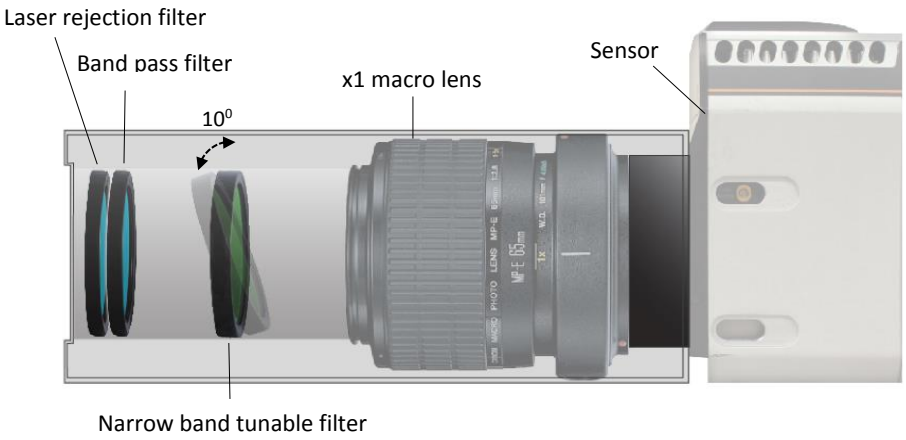

Figure 20. Imaging system schematics.

Imaging system schematics: Intensified CCD camera sensor records 1 cm field of view images of a single wavelength band through set of optical filters. The tunable Raman filter in the heart of the system transmits 849 nm emission at 10 degrees pivot rotation and 852 nm emission at 0 degrees – perpendicular to the optical axes. Front filters include 785 nm laser rejection filter and a band pass filter reducing broad fluorescence signals. This compact imaging setup utilizes off the shelf parts: Macro lens, optical filters and a near infra-red sensor.

The Raman peak bandwidth is proportional to the laser linewidth and exhibits ~1.6 nm emission bandwidth. Although the tunable filter has broader transmission spectra than the Raman peak, good differentiation between muscle and bone is achieved due to lower muscle and bone fluorescence signals, compared with the high intensity bone peak. Further improvement in bone mapping and sensitivity can be achieved by utilizing a 2 nm bandwidth detection window.

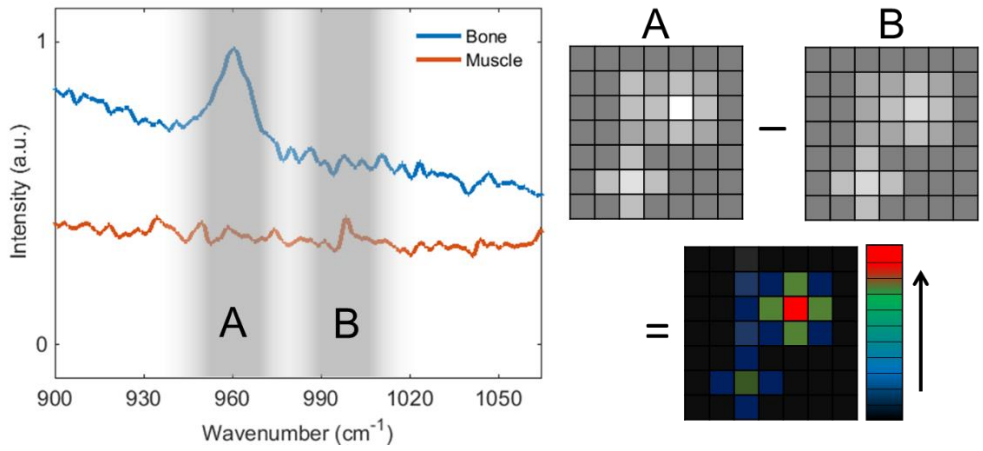

Figure 21. Fluorescence and Raman spectrum and imaging algorithm

Fluorescence and Raman spectrum of cortical bone and muscle tissues (left) with two imaging bands; A and B. Bone spectra shows the unique Raman signature of the phosphate at 960 cm^{-1} (Raman shift). Bone and muscle spectrum intensities realigned for better visualization. Image subtraction (right) removes the broad fluorescence signals (image B) and results in Raman map of bone locations.

The two images, each at different wavelength, hold sufficient information to localize the unique Raman signatures of bone by image subtraction. This composite image represents a 2D map of the bone locations. Tomographic approach implementation is required in order to resolve embedded bone structures in tissue beyond 5 mm depth, in order to resolve distance and size features. The adipose tissue and cortical bone selected for this experiment were taken from a food-grade bovine sample. No Institutional Review Board approval was required. 1 mm bone segments were chosen to represent the detection size limit (slice width) of medical x-ray (CT) systems. The x-ray scans

were taken by a high-resolution microCT (SkyScan 1172, Bruker MicroCT N.V., Kontich, Belgium) at an image resolution of 27.4 µm (70 kV and 141 µA radiation source, using a 0.5mm aluminum filter), and imaged using DataViewer software provided by the manufacturer.

Results

Our proof of concept macro-imaging Raman system is adapted to acquire full field images of tissue in real time without resolving Raman spectra, to capture the location of bone tissue structures (Figure 22). By using the unique Raman stokes signature of the Phosphate (PO_4^{3-}), specifically the tetrahedral symmetric stretching of the P-O bonds [1–4], a successful detection of the inorganic constituent within the bone structure is possible. Phosphate is a major building block of hydroxyapatite, the calcium mineral found in bone and heterotopic ossification, and is not found in significant quantities in other tissues. This signal can overcome the broad fluorescence background found in bone and tissue, and ultimately can enable in vivo detection. The spectra and algorithm are depicted in the methods section (Figure 21).

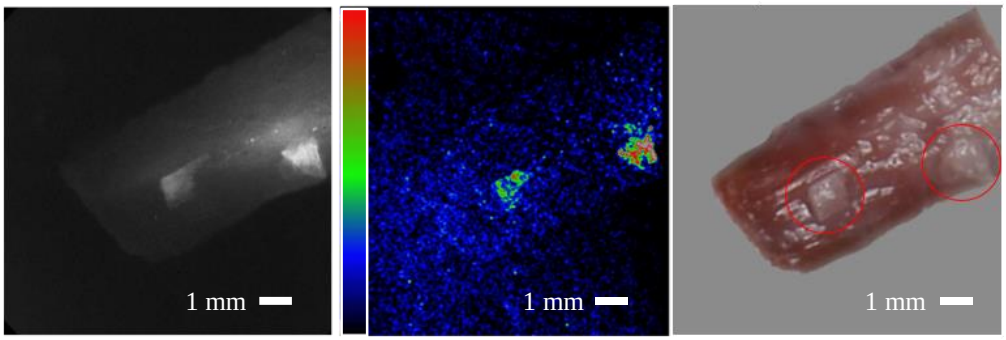

Figure 22. Bone on tissue imaging

Bone on tissue imaging. Right: Conventional color image taken after the experiment showing the tissue sample with 2 pieces of bone on top encircled in red, image rotated on grey background to match fluorescence and Raman images orientation. Adipose tissue and cortical bone fragments were taken from bovine samples. Left: Grey scale image of the fluorescence and Raman signals at optical wavelength of 852 nm (excitation wavelength is at 785 nm), showing both the bone and the soft tissue fluorescence signals. Middle: Raman signal computed image showing the bone locations. The muscle tissue fluorescence signal reduced significantly and showing close to background signal level. Bone signal is measured at about x10 larger than the surrounding tissue, which translate to 20 dB in Signal to Noise Ratio (SNR). Image threshold has been applied, due to laser beam non-uniformity signal levels from the two bone pieces at the two locations are different. Field of view in all images is 1 cm x 1 cm.

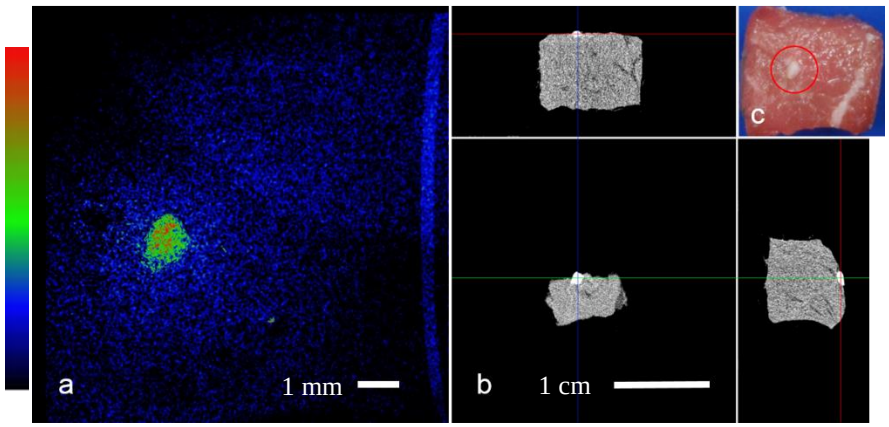

Figure 23. Bone on tissue imaging with microCT projections

Bone on tissue imaging: a. Top view Raman computed image of the tissue sample field of view is 1 cm. b. microCT projections of the sample, top and perpendicular side views. c. Top view color image with bone fragment encircled in red, bone size is ~1 mm.

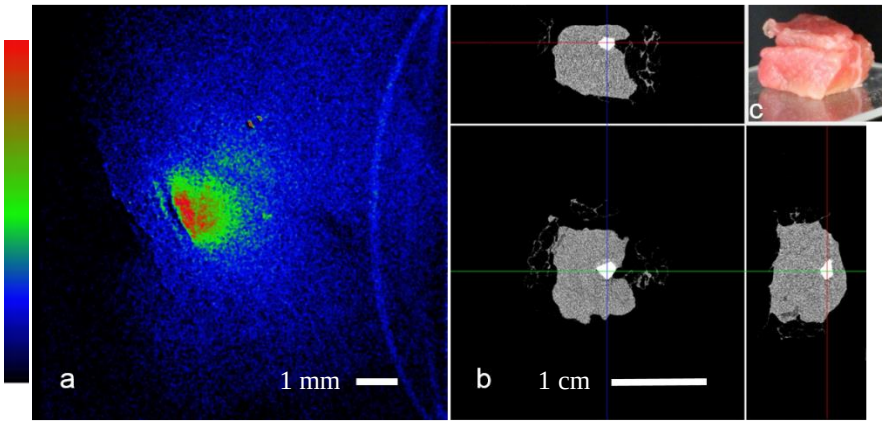

Figure 24. Bone embedded in tissue imaging with microCT projections

Bone embedded in tissue: a. Raman computed image of the tissue sample, the bone (~1 mm in size) Raman signal scattered through the top layer showing diffused boundaries and effectively

lowering resolution, field of view is 1 cm. b. microCT projections of the sample, top and perpendicular side views, scale bar 1 cm. c. Angled side view color image, showing top layer of meat (~2 - 3 mm thickness), and a bottom piece (~8 mm).

Further experiments conducted with collaboration of the dental school enabled validation of the imaging results using a microCT scanner (Figure 23, Figure 24). These experiments provide support for our imaging approach. These preliminary results show that we can detect a 1 mm bone fragment through 3 mm of bovine adipose tissue. The imaging result in Figure 22 was acquired using the ICCD, with 2 seconds total acquisition time. The ICCD's built-in image intensifier enables fast imaging with high sensitivity, however, the resulting images exhibit lower effective resolution due to the amplification process. Results in Figure 23 & Figure 24 were taken using the NIR camera with acquisition time of 8 seconds. This camera acquired higher resolution images with longer exposure times due to lack of signal amplification. Both cameras achieve similar SNR (with different noise characteristics) and are capable in producing acceptable results. The preferred sensor will depend on specific imaging needs including; determination of the required imaging speed, ease of implementation, and cost. These considerations will be better defined in future research efforts.

Conclusions

The direct Raman detection system has potential to detect bone Raman signals in vitro with settings that comply with in vivo conditions both in illumination intensity and speed. Further experiments are required in order to find the detection limits with respect to bone size and depth. Using trabecular bone (spongy bone) samples with lower hydroxyapatite concentration is planned in order to better simulate HO conditions. This will require an increase in the illumination power that can enable larger illumination area and offer better beam uniformity. Variable illumination and acquisition orientation can also be implemented in a tomographic imaging routine in order to better localize in-depth bone tissue locations.

Acknowledgements

We thank Dr. Kang Ting for providing the microCT scans, Justine Tanjaya for experimental support, and Chris Campillo from Andor Technology for loaning the NIR camera. This work was sponsored by the DoD Telemedicine & Advanced Technology Research Center (TATRC), grant# W81XWH-12-2-0075.

References

1. T. Buchwald, K. Niciejewski, M. Kozielski, M. Szybowicz, M. Siatkowski, and H. Krauss, "Identifying compositional and structural changes in spongy and subchondral bone from the hip joints of patients with osteoarthritis using Raman spectroscopy," J. Biomed. Opt. **17**, 0170071–0170077 (2012).
2. A. Hashimoto, L. Chiu, K. Sawada, T. Ikeuchi, K. Fujita, M. Takedachi, Y. Yamaguchi, S. Kawata, S. Murakami, and E. Tamiya, "In situ Raman imaging of osteoblastic mineralization," J. Raman Spectrosc. **45**, 157–161 (2014).
3. S. R. Goodyear, I. R. Gibson, J. M. S. Skakle, R. P. K. Wells, and R. M. Aspden, "A comparison of cortical and trabecular bone from C57 Black 6 mice using Raman spectroscopy," Bone **44**, 899–907 (2009).
4. N. J. Crane, E. Polfer, E. A. Elster, B. K. Potter, and J. A. Forsberg, "Raman spectroscopic analysis of combat-related heterotopic ossification development," Bone **57**, 335–342 (2013).
5. T. A. Davis, F. P. O'Brien, K. Anam, S. Grijalva, B. K. Potter, and E. A. Elster, "Heterotopic ossification in complex orthopaedic combat wounds: quantification and characterization of osteogenic precursor cell activity in traumatized muscle," J. Bone Joint Surg. Am. **93**, 1122–1131 (2011).
6. J. A. Forsberg and B. K. Potter, "Heterotopic ossification in wartime wounds," J. Surg. Orthop. Adv. **19**, 54–61 (2010).
7. M. B. K. Potter, "Heterotopic Ossification Following Combat-Related Trauma," J. Bone Jt. Surg. Am. **92**, 74 (2010).

8. J. A. Forsberg, B. K. Potter, E. M. Polfer, S. D. Safford, and E. A. Elster, "Do Inflammatory Markers Portend Heterotopic Ossification and Wound Failure in Combat Wounds?," Clin. Orthop. Relat. Res. **472**, 2845–2854 (2014).

9. J. R. Peterson, P. I. Okagbare, S. De La Rosa, K. E. Cilwa, J. E. Perosky, O. N. Eboda, A. Donneys, G. L. Su, S. R. Buchman, P. S. Cederna, S. C. Wang, K. M. Kozloff, M. D. Morris, and B. Levi, "Early detection of burn induced heterotopic ossification using transcutaneous Raman spectroscopy," Bone **54**, 28–34 (2013).

10. L. Nissim and D. Gilbertson-Dahdal, "An Unusual Complication of an Infiltrated Intravenous Catheter: Heterotopic Ossification in a Newborn," J. Radiol. Case Rep. **2**, 13–15 (2008).

11. B. P. Flannery, H. W. Deckman, W. G. Roberge, and K. L. D'Amico, "Three-Dimensional X-Ray Microtomography," Science **237**, 1439–1444 (1987).

12. M. G. M. Hunink and G. S. Gazelle, "CT screening: a trade-off of risks, benefits, and costs," J. Clin. Invest. **111**, 1612–1619 (2003).

13. M. V. Schulmerich, J. H. Cole, K. A. Dooley, M. D. Morris, J. M. Kreider, S. A. Goldstein, S. Srinivasan, and B. W. Pogue, "Non-invasive Raman tomographic imaging of canine bone tissue," J. Biomed. Opt. **13**, 020506 (2008).

14. J.-L. H. Demers, F. W. L. Esmonde-White, K. A. Esmonde-White, M. D. Morris, and B. W. Pogue, "Next-generation Raman tomography instrument for non-invasive in vivo bone imaging," Biomed. Opt. Express **6**, 793–806 (2015).

15. Y. Oshima, H. Sato, H. Kajiura-Kobayashi, T. Kimura, K. Naruse, and S. Nonaka, "Light sheet-excited spontaneous Raman imaging of a living fish by optical sectioning in a wide field Raman microscope," Opt. Express **20**, 16195 (2012).

16. H. R. Morris, C. C. Hoyt, P. Miller, and P. J. Treado, "Liquid Crystal Tunable Filter Raman Chemical Imaging," Appl. Spectrosc. **50**, 805–811 (1996).

17. J. Zhao, H. Lui, D. I. McLean, and H. Zeng, "Integrated real-time Raman system for clinical in vivo skin analysis," Skin Res. Technol. **14**, 484–492 (2008).

18. C. W. Freudiger, W. Min, B. G. Saar, S. Lu, G. R. Holtom, C. He, J. C. Tsai, J. X. Kang, and X. S. Xie, "Label-Free Biomedical Imaging with High Sensitivity by Stimulated Raman Scattering Microscopy," Science **322**, 1857–1861 (2008).

19. E. V. Efremov, J. B. Buijs, C. Gooijer, and F. Ariese, "Fluorescence rejection in resonance Raman spectroscopy using a picosecond-gated intensified charge-coupled device camera," Appl. Spectrosc. **61**, 571–578 (2007).

20. A. F. Palonpon, J. Ando, H. Yamakoshi, K. Dodo, M. Sodeoka, S. Kawata, and K. Fujita, "Raman and SERS microscopy for molecular imaging of live cells," Nat. Protoc. **8**, 677–692 (2013).

Future efforts

The fluorescence lifetime imaging system is currently used for *ex vivo* and *in vivo* imaging of various tissue types with ten band-pass filters that span the visible spectrum. The amount of data produced from each experiment is vast as each tissue type, filter, and the possible correlation between different filters contributes to the multi-dimensional dataset of the relative lifetime maps. The main goal would then be to reduce the amount of filters while optimizing the optical band-pass of the selected filters. Filters that exhibit similar information in *ex vivo* and *in vivo* experiments can be combined, for example, to improve photon efficiency and imaging speed. Another optimization method that could be employed is adding a secondary excitation wavelength. This can increase specificity in tissue identification and exclude unwanted biomarkers from the lifetime map, such as blood. These optimizations could improve tissue contrast generation and delineation of abnormal tissue intraoperatively.

The Raman Stokes wide-field system still needs to pass the proof of concept stage, and effectiveness *in vivo* has to be explored and validated. Few optimizations, including increased laser power and improved beam uniformity, are planned as well as techniques to increase the Raman signal over the fluorescence background such as time gated acquisition. The imaging capabilities through diffusive media, (muscle and particularly skin) is limited and structured illumination method can potentially resolve depth and size information of bony masses in tissue.

Finally, a dual modality, compact, single aperture camera design utilizing Fluorescence-Raman excitation and recording scheme can potentially be used for HO detection. Figure 25 shows the spectral bands of the two systems, both excitation and recording bands are displayed. A system

that can record and excite simultaneously Fluorescence and Raman signals can be constructed due to the low optical bandwidth cross-talk. A dual detector scheme, each recording a specific optical wavelength band, can be used for this task.

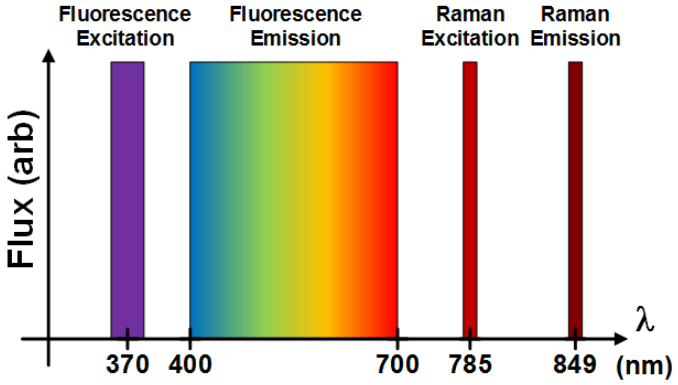

Figure 25. Raman and Fluorescence spectra utilization